Journal of Computational Physics **175,** 128–167 (2002)
doi:10.1006/jcph.2001.6931, available online at http://www.idealibrary.com on IDEAL®

A Free-Lagrange Augmented Godunov Method for the Simulation of Elastic–Plastic Solids

B. P. Howell* and G. J. Ball†

**Century Dynamics Ltd., Dynamics House, Hurst Road, Horsham, West Sussex, RH12 2DT, United Kingdom; and †School of Engineering Sciences, University of Southampton, Highfield, Southampton, Hampshire, SO17 1BJ, United Kingdom*
E-mail: gjb1@soton.ac.uk

Received December 28, 2000; revised August 13, 2001

A Lagrangian finite-volume Godunov scheme is extended to simulate two-dimensional solids in planar geometry. The scheme employs an elastic–perfectly plastic material model, implemented using the method of radial return, and either the 'stiffened' gas or Osborne equation of state to describe the material. The problem of mesh entanglement, common to conventional two-dimensional Lagrangian schemes, is avoided by utilising the free-Lagrange Method. The Lagrangian formulation enables features convecting at the local velocity, such as material interfaces, to be resolved with minimal numerical dissipation. The governing equations are split into separate subproblems and solved sequentially in time using a time-operator split procedure. Local Riemann problems are solved using a two-shock approximate Riemann solver, and piecewise-linear data reconstruction is employed using a MUSCL-based approach to improve spatial accuracy. To illustrate the effectiveness of the technique, numerical simulations are presented and compared with results from commercial fixed-connectivity Lagrangian and smooth particle hydrodynamics solvers (AUTODYN-2D). The simulations comprise the low-velocity impact of an aluminium projectile on a semi-infinite target, the collapse of a thick-walled beryllium cylinder, and the high-velocity impact of cylindrical aluminium and steel projectiles on a thin aluminium target. The analytical solution for the collapse of a thick-walled cylinder is also presented for comparison. © 2002 Elsevier Science

Key Words: free-Lagrange method; elastic–plastic solids; numerical simulation; Godunov method; time-operator splitting.

1. INTRODUCTION

This paper describes a new free-Lagrange numerical scheme (*Vucalm–EP*) that has been developed in order to simulate high-rate elastic–plastic deformation of materials with strength (i.e., the ability to withstand shear distortion). Traditionally, simulations such as

0021-9991/02 $35.00
© 2002 Elsevier Science
All rights reserved.

armour penetration and hypervelocity impact have been performed using space-centred finite-difference or finite-element schemes requiring artificial viscosity to control numerical oscillations. Large deformation problems have typically required Eulerian or arbitrary Lagrangian Eulerian (ALE) schemes incorporating some additional algorithm for tracking material interfaces, or complex interaction or slideline logic, respectively. Smooth particle hydrodynamics (SPH) schemes offer an alternative, grid-free method but are relatively diffusive. It has therefore been the objective of this work to investigate an alternative, fully Lagrangian, finite-volume approach for this type of simulation. By formulating the governing equations in the Lagrangian reference frame, the need to evaluate convective fluxes is avoided, thus eliminating a major source of numerical diffusion. As a result, features convecting at the local material velocity, such as material interfaces, are resolved sharply at all times without recourse to interface tracking. The tangling of conventional fixed-connectivity Lagrangian meshes is here avoided by utilising the free-Lagrange method (see Fritts *et al.* [12]), in which the computational mesh maintains fully Lagrangian motion, but the mesh connectivity is allowed to evolve in order to accommodate large material distortions. A cell-centred finite-volume formulation is used which enables the implementation of a Godunov-type solver in order to solve the hyperbolic component of the system.

High-order Godunov-type schemes have become commonplace for unsteady, inviscid, compressible gas dynamic calculations since they provide excellent shock-capturing capability combined with relatively low numerical diffusion. However, the application of such methods to materials with strength has been rare, due perhaps to the increased complexity of the Riemann problem resulting from the required material models and equations of state. For example, Tang and Ting [34] found that, in hyperelastic materials, the Riemann solution could contain composite nonlinear wave families in which a shock is in contact with a rarefaction of the same family. Wave systems consisting of two, three, and even four wave families instead of the usual three, where each individual family may be a simple rarefaction fan, a shock wave, or a composite wave, were also found to be common. Despite this increased complexity, the Riemann problem for the longitudinal and transverse motion in an elastic string has been solved by Keyfitz and Kranzer [19], and for the longitudinal motion in a strain-softening material by Shearer [30]. Also, Lin and Ballmann [20] present an interesting study detailing the construction of a second-order Godunov method for the numerical computation of elastic–plastic waves in thin-walled tubes. Trangenstein and Pember [38], when investigating the influence of plasticity, found that the analytical solution of the Riemann problem for the Antman–Szymczak model (a simple model describing longitudinal motion in an elastic–plastic bar which ignores body forces, transverse displacements, and thermal effects) reveals a total of 21 different wave systems, compared to the possible 10 for the Euler equations. This situation would be complicated still further if tensile failure were to be included. Using this experience, and motivated by the work of Liu [21] and Wendroff [44], Trangenstein and Colella [37] construct an extension of a second-order Godunov method to enable modelling of finite deformation in elastic–plastic solids. More recently, Miller and Puckett [22], and Tang and Sotiropoulos [33], discuss high-order Godunov methods for multiple condensed phases described using a Mie–Grüneisen equation of state and linear shock Hugoniot, and a hydro–elasto–plastic solid model, respectively.

Another high-order Godunov scheme recently developed for the simulation of elastic–plastic solids is due to Miller and Colella [23]. Utilising the deformation gradient, Miller and Colella [23] are able to obtain an Eulerian formulation of the governing equations of solid mechanics as a first-order system of hyperbolic partial differential equations. Since

the formulation introduces source terms, a predictor–corrector scheme is developed to solve the system. First a sophisticated second-order Godunov method provides a solution that is then modified to include the influence of the source terms. The Miller and Colella [23] scheme begins by forming van Leer limited gradients of the cell-centred variables, namely density, velocity, specific internal energy, the inverse of the deformation gradient, the plastic deformation tensor, a work hardening parameter, and the components of the Cauchy stress. A Riemann problem is then formed at the edge of a cell from the exact solution of the linearised equations. The Riemann problem is approximated using the eigenvectors of the coefficients of the linearised one-dimensional equations and preliminary conservative updates of the cell-centred variables are obtained. The final solution at time level $(n + 1)$ is then obtained with modification of the preliminary updates due to the presence of the source terms.

The present work differs from these previous studies in that operator splitting is used in order to avoid the additional complexities associated with inclusion of material strength in the Riemann problem. Since the total stress tensor conveniently decomposes into a deviatoric stress tensor, responsible for the strength of the material, and an isotropic hydrostatic pressure, the system of governing equations can readily be solved sequentially in time. The technique employed here is similar to the schemes discussed in Yanenko's method of fractional steps [46], which are often used in the solution of the Navier–Stokes equations (see Armfield and Street [1]). Similar techniques, referred to as time-operator or convection–diffusion split schemes, have been successfully employed to extend Godunov-type methods to solve viscous flows (see Toro and Brown [35] and Batten *et al.* [4]). The authors believe such an approach provides a sound foundation for the inclusion of more sophisticated material models. The utilisation of a free-Lagrange mesh also distinguishes the present study from traditional Lagrangian schemes such as presented by Caramana *et al.* [7, 9]. The free-Lagrange mesh and cell-centred formulation also allows for general topology, and arbitrary and automatically updated connectivity, without the problems of hourglassing common to other Lagrangian staggered-mesh schemes (see Caramana [6] and Caramana and Shashkov [8]).

The remainder of this paper is arranged thus: In the next section the numerical scheme, the development of which has been the main thrust of this work, is presented. First the governing equations are introduced, followed by a discussion of the decomposition of the total stress tensor, the elastic–perfectly plastic model, and the equations of state employed. The principle of time-operator splitting is discussed in Section 3.2 and the separate numerical operators are described in the remainder of Section 3. In Section 4 a selection of calculations are performed using our method, and these are compared to analytical solutions and results obtained using alternative techniques. Finally, in Section 5 we present our conclusions.

2. GOVERNING EQUATIONS

2.1. Equations of Motions

The governing equations for a continuous two-dimensional, homogeneous, nonheat conducting media are, in integral form,

$$\frac{\partial}{\partial t}\int_{V(t)} \mathbf{U}\, dV + \oint_{S(t)} \hat{\mathbf{n}} \cdot \mathbf{F}\, dS = 0, \tag{1}$$

where $V(t)$ is a time-dependent control volume enclosed by the boundary $S(t)$, $\mathbf{U}$ is the vector of conserved variables, and $\mathbf{F}$ is the flux vector. In the Lagrangian reference frame these vectors are

$$\mathbf{U} = \begin{bmatrix} 1 \\ \rho\mathbf{u} \\ \rho E \end{bmatrix} \quad \text{and} \quad \mathbf{F} = \begin{bmatrix} -\mathbf{u} \\ -\underline{\boldsymbol{\sigma}} \\ -\mathbf{u}\cdot\underline{\boldsymbol{\sigma}} \end{bmatrix}, \tag{2}$$

where ρ is the density, E is the total specific energy ($E = e + (\mathbf{u}\cdot\mathbf{u})/2$), e is the specific internal energy, $\underline{\boldsymbol{\sigma}}$ is the total stress tensor, and $\mathbf{u}$ is the vector velocity. (1) and (2) provide statements for the conservation of volume, momentum, and energy. In the Lagrangian reference frame, since no mass is exchanged between individual control volumes, the continuity equation in its usual form becomes redundant and is therefore replaced with an expression for the conservation of volume. For a material exhibiting strength the total stress can be decomposed into a hydrostatic, isotropic pressure p and a deviatoric stress tensor $\underline{\mathbf{s}}$, such that

$$\underline{\boldsymbol{\sigma}} = -p\underline{\mathbf{I}} + \underline{\mathbf{s}}, \tag{3}$$

where $\underline{\mathbf{I}}$ is the unit tensor and $\underline{\mathbf{s}}$ is the deviatoric stress tensor constructed thus—

$$\underline{\mathbf{s}} = \begin{bmatrix} s_x & s_{xy} \\ s_{xy} & s_y \end{bmatrix}, \tag{4}$$

where s_x, s_y are the direct stresses and s_{xy} is the shear stress. Such a decomposition of the total stress tensor leads to a convenient formulation of the governing equations,

$$\frac{\partial}{\partial t}\int_{V(t)} \mathbf{U}\,dV + \oint_{S(t)} \hat{\mathbf{n}}\cdot\mathbf{F}_{hydro}\,dS + \oint_{S(t)} \hat{\mathbf{n}}\cdot\mathbf{F}_{stren}\,dS = 0, \tag{5}$$

where $\mathbf{F}_{hydro}$ and $\mathbf{F}_{stren}$ are fluxes dependent on the hydrostatic pressure and on the state of deviatoric stress in the material, respectively. These fluxes are

$$\mathbf{F}_{hydro} = \begin{bmatrix} -\mathbf{u} \\ p\underline{\mathbf{I}} \\ \mathbf{u}p \end{bmatrix} \quad \text{and} \quad \mathbf{F}_{stren} = \begin{bmatrix} 0 \\ -\underline{\mathbf{s}} \\ \mathbf{u}\cdot\underline{\mathbf{s}} \end{bmatrix}. \tag{6}$$

Alternatively, utilising operator splitting, (5) becomes the two separate subproblems

$$\frac{\partial}{\partial t}\int_{V(t)} \mathbf{U}\,dV + \oint_{S(t)} \hat{\mathbf{n}}\cdot\mathbf{F}_{hydro}\,dS = 0 \tag{7}$$

and

$$\frac{\partial}{\partial t}\int_{V(t)} \tilde{\mathbf{U}}\,dV + \oint_{S(t)} \hat{\mathbf{n}}\cdot\mathbf{F}_{stren}\,dS = 0. \tag{8}$$

In the scheme developed here (7) and (8) are solved sequentially in time using a time-operator splitting procedure to be described in Section 3; hence $\tilde{\mathbf{U}}$ signifies an intermediate value of the vector of conserved variables resulting from the solution of (7) alone. In order to complete the description, a material model is required consisting of a constitutive model relating deformation to the state of deviatoric stress and an equation of state to quantify volumetric response.

2.2. Elastic–Perfectly Plastic Solid

Using the generalised Hooke's law [42], the relationship between stress σ and strain ϵ for a continuous isotropic material in the principal directions (1, 2, 3) is

$$\begin{aligned} \sigma_1 &= \lambda\varepsilon + 2\mu\epsilon_1 \\ \sigma_2 &= \lambda\varepsilon + 2\mu\epsilon_2 \\ \sigma_3 &= \lambda\varepsilon + 2\mu\epsilon_3, \end{aligned} \tag{9}$$

where $\varepsilon = \epsilon_1 + \epsilon_2 + \epsilon_3$ is the volumetric strain and λ and μ are the constants of Lamé. Furthermore,

$$\mu = G, \quad \lambda = \frac{\nu E}{(1+\nu)(1-2\nu)}, \tag{10}$$

where G is the shear modulus, E is Young's modulus, and ν is Poisson's ratio. Transforming between principal stress space and an orthogonal Cartesian (x, y) coordinate system and simplifying to two dimensions, Hooke's law yields

$$\begin{aligned} \sigma_x &= \lambda\varepsilon + 2\mu\epsilon_x \\ \sigma_y &= \lambda\varepsilon + 2\mu\epsilon_y \\ \tau_{xy} &= \mu\epsilon_{xy}, \end{aligned} \tag{11}$$

where σ_x, σ_y, ϵ_x, ϵ_y are the normal stresses and strains in the x and y directions, respectively; τ_{xy} and ϵ_{xy} are the shear stress and strain; and $\varepsilon = \epsilon_x + \epsilon_y + \epsilon_z = \epsilon_1 + \epsilon_2 + \epsilon_3$ since the sum of the longitudinal strain components is invariant with the transformation of the coordinate axes. Moreover, since $\dot{\sigma}_x = -\dot{p} + \dot{s}_x$ and the hydrostatic pressure can be defined as the mean of the three stresses $p = -1/3(\sigma_x + \sigma_y + \sigma_z)$, the deviatoric stress can be represented

$$\dot{s}_x = 2\mu\dot{\epsilon}_x - \frac{2}{3}\mu(\dot{\epsilon}_x + \dot{\epsilon}_y + \dot{\epsilon}_z), \tag{12}$$

since $\dot{\sigma}_x = \lambda\dot{e} + 2\mu\dot{\epsilon}_x$, where the dot denotes a time derivative along a particle path. Thus, Hooke's law can be written is terms of differential deviatoric stress,

$$\begin{aligned} \dot{s}_x &= 2\mu(\dot{\epsilon}_x - \dot{v}/3v) \\ \dot{s}_y &= 2\mu(\dot{\epsilon}_y - \dot{v}/3v) \\ \dot{s}_{xy} &= \mu\dot{\epsilon}_{xy}, \end{aligned} \tag{13}$$

where, from a consideration of continuity,

$$\frac{\dot{v}}{v} = \dot{\epsilon}_x + \dot{\epsilon}_y + \dot{\epsilon}_z, \tag{14}$$

where v denotes the specific volume. Hence, (13) completely describes the state of deviatoric stress for an elastic, two-dimensional, isotropic material as a function of its deformation. To model an elastic–plastic material an additional yield condition is required which defines the material elastic limit and hence determines when plastic flow occurs. For the present

work, the von Mises yield condition has been employed, which can be written in terms of the principal stresses,

$$(\sigma_1 - \sigma_2)^2 + (\sigma_2 - \sigma_3)^2 + (\sigma_3 - \sigma_1)^2 = 2(Y^0)^2, \tag{15}$$

where Y^0 is the yield strength of the material in simple tension. With transformation into the two-dimensional Cartesian (x, y) coordinate system, and using (3), the yield condition can be written as

$$s_x^2 + s_y^2 + 2s_{xy}^2 \leq \frac{2}{3}(Y^0)^2, \tag{16}$$

and it is this expression which is used to detect the onset of plastic flow. In the numerical scheme discussed in this work, once yield is detected the material is assumed to flow plastically, resisting with a constant state of deviatoric stress; hence the term elastic–perfectly plastic. Finally, an equation of state relating the pressure to density and internal energy is required to complete the material model.

2.3. Equation of State

Two equations of state (EOS) have been employed in the present work; the 'stiffened gas' EOS (see Tyndall [39], Harlow and Amsden [16], and Weixen [43]) and the quadratic Osborne EOS (see Riney [28]). The 'stiffened gas' EOS is a simplification of the more general Mie–Grüneisen EOS. It provides a fair approximation to the behaviour of solids, providing that the departures from the reference density are slight, and has the form

$$p = c_0^2(\rho - \rho_0) + (\gamma_0 - 1)\rho e, \tag{17}$$

where c_0 is the unshocked sound speed, ρ_0 is a reference density, e is the specific internal energy, and γ_0 is the Grüneisen gamma. The Osborne EOS has the form

$$p_{osb} = \frac{a_1\eta + \bar{a}\eta^2 + E'(b_0 + b_1\eta + b_2\eta^2) + E'^2(c_0 + c_1\eta)}{E' + e_0}, \tag{18}$$

where $\eta = \rho/\rho_0 - 1$, $E' = e\rho_0$, and

$$\bar{a} = \begin{cases} a_2, & \eta \geq 0 \\ a_2^*, & \eta < 0. \end{cases} \tag{19}$$

For the Osborne EOS, a minimum pressure is imposed such that the actual pressure is taken as $p = \max(p_{min}, p_{osb})$, where $a_1, a_2, a_2^*, b_0, b_1, b_2, c_0, c_1, e_0$, and p_{min} are material-dependent parameters. All that remains in the constitutive model is to obtain an expression for the local sound speed in the material for each EOS. Recalling that for all equations of state,

$$c^2 = \left(\frac{\partial p}{\partial \rho}\right)_e + \frac{p}{\rho^2}\left(\frac{\partial p}{\partial e}\right)_\rho, \tag{20}$$

therefore for the 'stiffened gas' EOS an expression for the sound speed can easily be derived thus:

$$c^2 = c_0^2 + (\gamma_0 - 1)\left[e + \frac{p}{\rho}\right]. \tag{21}$$

And for the Osborne EOS, following some differentiation,

$$\left(\frac{\partial p}{\partial \rho}\right)_e = \frac{a_1 + 2\bar{a}\eta + E'(b_1 + 2\eta b_2 + E'c_1)}{\rho_0(E' + e_0)} \tag{22}$$

and

$$\left(\frac{\partial p}{\partial e}\right)_\rho = \frac{\rho_0(b_0 + b_1\eta + b_2\eta^2 + 2E'(c_0 + c_1\eta) - p)}{E' + e_0}. \tag{23}$$

Thus, the material model for two-dimensional, elastic–perfectly plastic flow employed here can be summarised as:

(i) decomposition of total stress $\begin{cases}\sigma_x = -p + s_x \\ \sigma_y = -p + s_y,\end{cases}$

(ii) differential stress-strain relationships $\begin{cases}\dot{s}_x = 2\mu(\dot{\epsilon}_x - \frac{1}{3}\frac{\dot{v}}{v}) \\ \dot{s}_y = 2\mu(\dot{\epsilon}_y - \frac{1}{3}\frac{\dot{v}}{v}), \\ \dot{s}_{xy} = \mu\dot{\epsilon}_{xy}\end{cases}$ (24)

(iii) von Mises yield condition $s_x^2 + s_y^2 + 2s_{xy}^2 \le \frac{2}{3}(Y^0)^2$,

(iv) flow rule—(perfectly plastic), and

(v) equation of state $p = p(\rho, e)$.

In the next section the numerical procedure for implementing the material model is discussed.

3. NUMERICAL SCHEME

3.1. General Details

The numerical scheme described in this work is based on the two-dimensional computational fluid dynamics (CFD) code *Vucalm*, developed by Ball [2] for the solution of the unsteady, compressible Euler equations on an unstructured Lagrangian, finite-volume mesh.

At the beginning of a calculation a two-dimensional domain is defined which is filled with computational 'particles.' Associated with each particle is a material type, with appropriate material properties, the particle position (x, y), and the material conditions at that position. Based entirely on the particle positions, a Voronoi mesh is constructed which describes a unique tessellation of the domain using nonoverlapping polygonal cells. The Voronoi diagram is the geometric dual of the more commonly known Delaunay triangulation [13, 27]. Each cell encloses a single particle and contains the region on the computational plane closest to that particle, forming an associated material 'packet.' Mass exchange between

cells is forbidden, hence mass is conserved exactly at all times. The cells form the computational control volumes for the time integration of the governing equations. Once the material velocities, stored at the particle positions, are known at the new time level, they can be integrated in time to obtain the new particle positions. Hence the particles move in a purely Lagrangian fashion and are a permanent feature of a calculation. In contrast, the Voronoi mesh is ephemeral and may be reconstructed as often as desired, allowing the mesh connectivity to evolve freely in response to material deformation. In highly shearing materials the mesh may be reconstructed on every timestep or, in order to minimise CPU time, the user may opt to reconstruct less frequently (perhaps every 5 timesteps). During intervening timesteps the existing mesh vertices are convected at the local material velocity.

It is important to note at this juncture that it is a common misconception that reconstruction of the computational mesh introduces diffusion or a loss of conservation. Since all fluxes are conservative, and mass exchange between cells is forbidden, the quantities of mass, momentum, and energy are always conserved. Furthermore, the mesh reconstruction, unlike more common strategies such as ALE, involves no exchange of any property between individual cells; it merely constitutes an update of the local connectivity of the mesh and the estimated locations of the cell boundaries.

3.2. Solution Procedure

Utilising a time-operator splitting procedure the integration of the solution from time level t^n to t^{n+1} consists of two sequential steps. In the first 'hydrodynamic' step, (7) is solved, thus advancing the vector of conserved variables to an intermediate time level utilising a spatially second-order Godunov solver, i.e.,

$$\mathbf{U}^n \rightarrow \tilde{\mathbf{U}}. \tag{25}$$

Note that throughout this discussion the tilde overbar ($\sim$) represents intermediate solutions resulting from the hydrodynamic step. During this initial step the material is assumed to be without strength and the state of stress at time level t^n has no influence. In the second 'deviatoric' step the velocities from the intermediate solution are used to form velocity strains in order to integrate the differential stress–strain relations (13) and hence obtain a provisional update of the deviatoric stress tensor $\underline{\mathbf{s}}$, i.e.,

$$\underline{\mathbf{s}}^n \rightarrow \bar{\underline{\mathbf{s}}}, \tag{26}$$

where the plain overbar ($-$) indicates a provisional state resulting from the deviatoric step. A definitive update of the conserved variables is then obtained using the provisional state of deviatoric stress $\bar{\underline{\mathbf{s}}}$. Finally, time-centred velocity strains, formed from an average of velocities at time levels $\tilde{t}$ and t^{n+1}, are used to obtain a definitive update of the cell-centred deviatoric stress. This completes the timestep. The individual hydrodynamic and deviatoric operators are discussed in detail in the following sections.

3.3. Hydrodynamic Operator

The time stepping of (7) differs very little from that of a comparable Euler solver. Following Ball [2], the dependent variables at time level t^n and at the intermediate level are

related thus—

$$\tilde{\mathbf{U}} = \frac{\tilde{\rho}}{\rho^n}\left(\mathbf{U}^n - \frac{\rho^n \Delta t}{m}\sum_{k=1}^{K} \hat{\mathbf{n}}_k \cdot \mathbf{F}^n_{hydro_k} S_k\right), \tag{27}$$

where m is the control volume mass, Δt the timestep, and the subscript k indicates the kth side of the control volume. Thus, $\mathbf{F}_{hydro_k}$, S_k, and $\hat{\mathbf{n}}_k$ are the numerical flux, the side length, and the outward pointing normal vector, respectively, for the kth side of the computational cell. The density update is obtained by applying volume conservation as

$$\tilde{\rho} = \left(\frac{1}{\rho^n} + \frac{\Delta t}{m}\sum_{k=1}^{K} u^*_k S_k\right)^{-1}, \tag{28}$$

since

$$\tilde{V} = V^n + \Delta t \sum_{k=1}^{K} u^*_k S_k, \tag{29}$$

where V is the computational cell volume and u^*_k is the normal velocity directed out of the control volume. In (27), the numerical flux is required on each side of the computational cell and is formally found from $\mathbf{F}_{hydro_k} = \mathbf{A}\mathbf{F}^*_k$, where

$$\mathbf{A} = \begin{bmatrix} \hat{\mathbf{n}}_k & 0 & 0 \\ 0 & \underline{\mathbf{I}} & 0 \\ 0 & 0 & \hat{\mathbf{n}}_k \end{bmatrix}, \quad \mathbf{F}^*_k = \begin{bmatrix} -u^*_k \\ p^*_k \\ u^*_k p^*_k \end{bmatrix}, \tag{30}$$

where the superscript $*$ indicates wave-processed states at the cell boundary. These are obtained from the solution to the Riemann problem formed at the kth control volume side. Note that for a Lagrangian mesh, the cell boundary is coincident with the contact surface of the local Riemann problem, and hence the values of u^*_k, p^*_k are always determined at the contact surface. This represents a significant simplification relative to Eulerian Godunov schemes in which the cell boundary may lie anywhere within the local wave system, depending upon the local velocity and wave speeds.

The Riemann problem is an initial value problem with left (l) and right (r) input states constructed from an interpolation of the cell-centred primitive variables assuming a piecewise-linear reconstruction within each cell. Required inputs are density $\rho_{l,r}$, pressure $p_{l,r}$, and velocity normal to the cell face $u_{l,r}$. In order to ensure monotonicity, the gradients of primitive variables are limited using a MUSCL-based approach (see Ball [2] for algebraic details).

In the present work, the two nonlinear waves present in the Riemann solution are both assumed to be shock waves, and the Riemann solver of Dukowicz [11] has been employed to calculate the wave-processed states u^* and p^*. For a discussion of the two-shock approximation in the solution of the Riemann problem, see Toro [36]. The Dukowicz solver is attractive for this type of application because it provides an approximate noniterative Riemann solution for a broad class of materials characterised simply by the slope of the shock Hugoniot and the local sound speed. Though the exact solution for the stiffened gas EOS is readily obtainable (see Cocchi *et al.* [10] and Plohr [26]), it is felt that this approximate solver provides scope for the incorporation of more realistic EOS in the future. For

example, provided that an expression for the local sound speed can be obtained, there is no reason why a more accurate version of the Mie–Grüneisen EOS cannot be employed (see Gust [14] and Steinberg *et al.* [31]).

Once (27) and (28) have been used to obtain the intermediate values of the conserved variables, the particle positions can be updated by integrating the intermediate velocity $\tilde{\mathbf{u}}$. The intermediate conserved variable vector, $\tilde{\mathbf{U}}$, and the particle positions are now ready to form the initial conditions for the deviatoric step.

3.4. Deviatoric Operator

The deviatoric operator can be conveniently divided into three distinct stages which are discussed in the following sections.

3.4.1. *Stage 1: Predicted Cell-Centred Stress*

The first stage of the deviatoric operator is to obtain a cell-centred prediction of the state of deviatoric stress in each control volume based on the intermediate hydrodynamic update $\tilde{\mathbf{U}}$. Numerically, (13) can be integrated in time to give a predicted state of deviatoric stress,

$$\begin{aligned}
\bar{s}_x &= s_x^n + \left[2\mu\left(\dot{\epsilon}_x - \frac{1}{3}\dot{\varepsilon}\right) + \delta_x\right]\Delta t \\
\bar{s}_y &= s_y^n + \left[2\mu\left(\dot{\epsilon}_y - \frac{1}{3}\dot{\varepsilon}\right) + \delta_y\right]\Delta t \\
\bar{s}_{xy} &= s_{xy}^n + [\mu\dot{\epsilon}_{xy} + \delta_{xy}]\Delta t,
\end{aligned} \tag{31}$$

where the velocity gradients yield the strain rates thus (see Wang [42]):

$$\begin{aligned}
\dot{\epsilon}_x &= \frac{\partial\tilde{u}}{\partial x}, \quad \dot{\epsilon}_y = \frac{\partial\tilde{v}}{\partial y} \\
\dot{\epsilon}_{xy} &= \frac{\partial\tilde{u}}{\partial y} + \frac{\partial\tilde{v}}{\partial x}, \quad \dot{\varepsilon} = \frac{\partial\tilde{u}}{\partial x} + \frac{\partial\tilde{v}}{\partial y}.
\end{aligned} \tag{32}$$

Here the velocity is assumed to vary linearly within each computational cell. Estimates of the velocity gradients for a given cell are obtained by fitting a plane surface to the cell-centred velocities of the K neighbouring cells, by least-squares, with the squared-error for each neighbour weighted by the shared side length S_k. Note that in (31), the additional terms δ_x, δ_y, and δ_{xy} appear. During two-dimensional displacement a material element may experience rotation in addition to distortion. Any rigid body rotation should not change the state of stress of the element but will constitute a transformation or redistribution of the deviatoric stress components. Thus, to ensure the stress–strain relationship remains independent of rigid body motion, the additional rigid body correction terms are introduced to allow for the coordinate transformation (see Wilkins [45]). The components of stress in an arbitrarily orientated orthogonal coordinate system (x', y') may be related to those in the (x, y) system by the transformation formulae

$$\begin{aligned}
s_{x'} &= s_x \cos^2\omega + s_y \sin^2\omega - s_{xy}\sin 2\omega \\
s_{y'} &= s_x \sin^2\omega + s_y \cos^2\omega + s_{xy}\sin 2\omega \\
s_{x'y'} &= \frac{1}{2}(s_x - s_y)\sin 2\omega + s_{xy}\cos 2\omega.
\end{aligned} \tag{33}$$

Therefore, if a body is rotated through an angle ω in the (x, y) plane during the timestep, the correction must be equal to the difference between the transformed stresses and the original stresses,

$$\begin{aligned} \delta_x &= s_{x'} - s_x \\ \delta_y &= s_{y'} - s_y \\ \delta_{xy} &= s_{x'y'} - s_{xy}. \end{aligned} \tag{34}$$

The rotation angle ω is obtained from an estimate of the vorticity of the material given by

$$\sin\omega = \frac{1}{2}\left[\frac{\partial\tilde{v}}{\partial x} - \frac{\partial\tilde{u}}{\partial y}\right]\Delta t. \tag{35}$$

Hence, at the end of Stage 1 a predicted state of deviatoric stress is available at particle positions throughout the computational domain. Next, this state of stress must be allowed to influence the conserved variables in each control volume.

3.4.2. *Stage 2: Material Strength Flux Calculation*

In order to determine the strength flux $\mathbf{F}_{stren}$, the state of deviatoric stress must be estimated at each cell face. Consider a given 'target' cell, with neighbours $k = 1..K$ (see Fig. 1). The predicted deviatoric stresses $\bar{s}_x, \bar{s}_y, \bar{s}_{xy}$ obtained in Stage 1 are assumed to vary linearly within each cell, with gradients obtained by least squares. The numerical flux on the kth face is constructed from an average of the predicted stress state linearly interpolated from the target (subscript $_T$) and neighbour particle positions and then orientated to the face coordinate system—see Fig. 1. The average stress states are obtained from

$$\bar{s}_{x_{avg}} = \frac{1}{2}\left(\bar{s}^{EI}_{x_T} + \bar{s}^{EI}_{x_k}\right), \quad \bar{s}_{y_{avg}} = \frac{1}{2}\left(\bar{s}^{EI}_{y_T} + \bar{s}^{EI}_{y_k}\right), \quad \bar{s}_{xy_{avg}} = \frac{1}{2}\left(\bar{s}^{EI}_{xy_T} + \bar{s}^{EI}_{xy_k}\right), \tag{36}$$

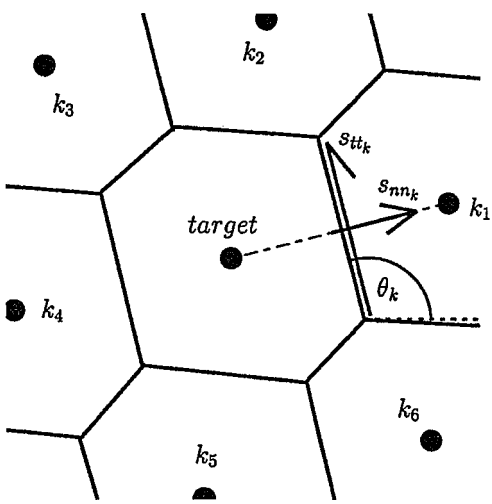

FIG. 1. Schematic illustrating the construction of edge-orientated normal and shear stresses for the $k = 1$ neighbour. s_{nn_k} is the normal deviatoric stress directed out of the 'target' cell, normal to the midpoint of the cell face shared with the $k = 1$ neighbour. s_{tt_k} is the shear stress acting tangential to the cell face, counterclockwise around the target cell. θ_k is the angle between the cell face and the positive x-axis.

where the edge interpolated states (superscript ^{EI}) are formed

$$\begin{aligned}
\bar{s}^{EI}_{x_T} &= \bar{s}_{x_T} + \frac{\partial \bar{s}_{x_T}}{\partial x}\Delta x_{Tk} + \frac{\partial \bar{s}_{x_T}}{\partial y}\Delta y_{Tk}, & \bar{s}^{EI}_{x_k} &= \bar{s}_{x_k} + \frac{\partial \bar{s}_{x_k}}{\partial x}\Delta x_{kT} + \frac{\partial \bar{s}_{x_k}}{\partial y}\Delta y_{kT} \\
\bar{s}^{EI}_{y_T} &= \bar{s}_{y_T} + \frac{\partial \bar{s}_{y_T}}{\partial x}\Delta x_{Tk} + \frac{\partial \bar{s}_{y_T}}{\partial y}\Delta y_{Tk}, & \bar{s}^{EI}_{y_k} &= \bar{s}_{y_k} + \frac{\partial \bar{s}_{y_k}}{\partial x}\Delta x_{kT} + \frac{\partial \bar{s}_{y_k}}{\partial y}\Delta y_{kT} \\
\bar{s}^{EI}_{xy_T} &= \bar{s}_{xy_T} + \frac{\partial \bar{s}_{xy_T}}{\partial x}\Delta x_{Tk} + \frac{\partial \bar{s}_{xy_T}}{\partial y}\Delta y_{Tk}, & \bar{s}^{EI}_{xy_k} &= \bar{s}_{xy_k} + \frac{\partial \bar{s}_{xy_k}}{\partial x}\Delta x_{kT} + \frac{\partial \bar{s}_{xy_k}}{\partial y}\Delta y_{kT},
\end{aligned} \tag{37}$$

where, for example, $\frac{\partial \bar{s}_{x_T}}{\partial x}$, $\frac{\partial \bar{s}_{x_k}}{\partial x}$ are the Cartesian gradients of the predicted deviatoric stresses in the target and kth neighbour cells, respectively. Here the displacements from the target and the kth neighbour, to the face midpoint, are

$$\begin{aligned}
\Delta x_{Tk} &= x_{mp} - x_T, \quad \Delta y_{Tk} = y_{mp} - y_T \\
\Delta x_{kT} &= x_{mp} - x_k, \quad \Delta y_{kT} = y_{mp} - y_k,
\end{aligned} \tag{38}$$

where $(x, y)_{mp}$, $(x, y)_T$, $(x, y)_k$ are the positions of the face midpoint, the target particle, and the kth neighbour, respectively.

The interpolated stress components are transformed into components normal and parallel to the cell face, using

$$\begin{aligned}
s_{nn_k} &= \bar{s}_{y_{avg}}\cos^2\theta_k + \bar{s}_{x_{avg}}\sin^2\theta_k - \bar{s}_{xy_{avg}}\sin 2\theta_k \\
s_{tt_k} &= \frac{1}{2}\left(\bar{s}_{x_{avg}} - \bar{s}_{y_{avg}}\right)\sin 2\theta_k + \bar{s}_{xy_{avg}}\cos 2\theta_k,
\end{aligned} \tag{39}$$

where θ_k is the angle between the face and the positive x-axis. Thus a definitive conservative update of the conserved variables can be obtained from

$$\mathbf{U}^{n+1} = \frac{\tilde{\rho}}{\rho^n}\left(\tilde{\mathbf{U}} - \frac{\rho^n \Delta t}{m}\sum_{k=1}^{k}\hat{\mathbf{n}}_k \cdot \mathbf{F}^n_{stren_k} S_k\right), \tag{40}$$

where the strength flux is formally constructed as

$$\mathbf{F}_{stren_k} = \begin{bmatrix} 0 \\ -n_x s_{nn_k} + n_y s_{tt_k} \\ -n_y s_{nn_k} - n_x s_{tt_k} \\ -u^*_k s_{nn_k} - u_{tt} s_{tt_k} \end{bmatrix}, \tag{41}$$

where n_x and n_y are the x- and y-wise components of the unit normal $\hat{\mathbf{n}}_k$ on the kth cell face and u^*_k and u_{tt} are the velocities normal and tangential to the cell face. Here u^*_k comes from the Riemann solution calculated in the hydrodynamic operator and u_{tt} from a linear interpolation of the local particle velocities. Note that on the current time step, material strength has no influence on the update of density, and hence $\rho^{n+1} = \tilde{\rho}$. However, the deviatoric operator does change the momentum and energy of the particle. These changes will modify the Riemann problem to be solved in the $(n+1)$th timestep, which will in turn influence the particle density. Having obtained a final update of the conserved variables, the definitive update of the cell-centred deviatoric stress can now be computed.

3.4.3. *Stage 3: Definitive Cell-Centred Stress Update*

The definitive cell-centred update of deviatoric stress is calculated in a fashion similar to that of the predicted stress (as described in Section 3.4.1), except that the strain rates and rigid body corrections are now time-centred (superscript *TC*) with respect to the deviatoric operator,

$$\begin{aligned} s_x^{n+1} &= s_x^n + \left[2\mu\left(\dot{\epsilon}_x^{TC} - \frac{1}{3}\dot{\varepsilon}^{TC}\right) + \delta_x^{TC}\right]\Delta t \\ s_y^{n+1} &= s_y^n + \left[2\mu\left(\dot{\epsilon}_y^{TC} - \frac{1}{3}\dot{\varepsilon}^{TC}\right) + \delta_y^{TC}\right]\Delta t \\ s_{xy}^{n+1} &= s_{xy}^n + \left[\mu\dot{\epsilon}_{xy}^{TC} + \delta_{xy}^{TC}\right]\Delta t, \end{aligned} \tag{42}$$

where

$$\begin{aligned} \dot{\epsilon}_x^{TC} &= \frac{1}{2}\left(\frac{\partial\tilde{u}}{\partial x} + \frac{\partial u^{n+1}}{\partial x}\right), \quad \dot{\epsilon}_y^{TC} = \frac{1}{2}\left(\frac{\partial\tilde{v}}{\partial y} + \frac{\partial v^{n+1}}{\partial y}\right) \\ \dot{\epsilon}_{xy}^{TC} &= \frac{1}{2}\left(\frac{\partial\tilde{u}}{\partial y} + \frac{\partial u^{n+1}}{\partial y}\right) + \frac{1}{2}\left(\frac{\partial\tilde{v}}{\partial x} + \frac{\partial v^{n+1}}{\partial x}\right) \\ \dot{\varepsilon}^{TC} &= \frac{1}{2}\left(\frac{\partial\tilde{u}}{\partial x} + \frac{\partial u^{n+1}}{\partial x}\right) + \frac{1}{2}\left(\frac{\partial\tilde{v}}{\partial y} + \frac{\partial v^{n+1}}{\partial y}\right). \end{aligned} \tag{43}$$

Hallquist has shown [15] that the time-centred strain rate is preferred for large deformation simulations, not only because it closely agrees with the true strain, but also because it avoids the erroneous calculation of nonzero strain rates during rigid body rotation.

Before the state of deviatoric stress calculated from (42) is accepted as the final stress state it must be tested against the yield condition. The von Mises yield condition, (15), is used in this work and is implemented using the method of radial return due to Wilkins [45]. The steps to impose the yield condition are:

(i) Compare the state of deviatoric stress with the yield condition. If $s_x^2 + s_y^2 + 2s_{xy}^2 \leq 2/3(Y^0)^2$ then response is elastic and this is the final state of stress. If $s_x^2 + s_y^2 + 2s_{xy}^2 > 2/3(Y^0)^2$ then material has yielded and flow is plastic; move to step (ii).

(ii) Radially rescale each stress component to lie on the yield surface by multiplying by the rescaling factor,

$$\frac{\sqrt{2/3}Y^0}{\sqrt{s_x^2 + s_y^2 + 2s_{xy}^2}}. \tag{44}$$

All that remains is to integrate the velocities to obtain new particle positions,

$$x^{n+1} = x^n + \frac{\Delta t}{2}(u^n + u^{n+1}), \quad y^{n+1} = y^n + \frac{\Delta t}{2}(v^n + v^{n+1}), \tag{45}$$

and to either convect or reconstruct the computational mesh for the beginning of the next timestep.

3.5. Treatment of Void Regions

Hydrocodes are often required to simulate problems, such as hypervelocity impact, in which the region surrounding the deforming projectile and target is a void (vacuum), or may be approximated as such. The way in which the void region is represented may be a significant issue in the design of an appropriate numerical scheme. In addition, the free surface of the deforming material will typically display large distortions. Mesh entanglement would normally terminate a fixed-connectivity Lagrangian calculation before large free surface distortions are reached. Problems also arise in ALE simulations if free surfaces 'roll-up' or turn back on themselves. Therefore, to simulate problems involving highly deforming free surfaces, Eulerian or SPH methods have generally been used in the past. In an Eulerian calculation, void regions are defined through which the materials of interest can convect. In contrast, the particle-based SPH technique does not require an enclosing computational mesh or grid and hence there is no requirement to explicitly represent void regions.

In the free-Lagrange scheme developed here, the materials of interest must always be enclosed within a global computational domain. Consequently, additional computational particles are required within the void region to ensure the computational mesh always fills the complete domain. Free surfaces are always coincident with cell boundaries between the additional *void particles* and those particles which constitute the materials of interest. The void particles are designed such that the materials of interest behave as if they are enclosed within a vacuum. Void particles are assigned a nonzero fictitious mass and an EOS, usually the same as the materials of interest, and are described by the same governing equations, (1) and (2), but with zero material strength, i.e., $\underline{\mathbf{s}} = 0$. Thus, only the hydrodynamic operator is required to describe the evolution of the void particles, and the standard solution procedure may be used, except at cell boundaries between the materials of interest and void particles.

In order for solid materials to behave as if enclosed within a vacuum, the following criteria must be fulfilled at solid/void cell boundaries:

(i) Void particles must have no influence on gradient estimates within computational cells containing solid material, and vice versa.

(ii) Void particles must do no work on, and impose no forces on, adjoining solid particles.

(iii) Movement of void particles must be such as to minimise the 'volumetric error' (see below) in adjoining solid particles.

For particles on a solid/void boundary, criterion (i) is met by simply excluding void particles when performing both gradient construction and slope limiting for solid particles, and vice versa. In order to satisfy criteria (ii) and (iii), modifications to the associated Riemann problems, and consequently the calculated flux (30), are required. It is important to note that different Riemann problems are solved at solid/void boundaries, depending on whether the target particle is solid or void, and hence at these boundaries the hydrodynamic flux $\mathbf{F}_{hydro_k}$ is not conservative. However, this is not of practical concern, since the thermodynamic volume, momentum, and energy are always accurately conserved within the materials of interest—conservation violations are restricted to the fictitious void particles.

To satisfy criterion (ii), no force must be allowed to act on cell faces shared between solid and void cells from the perspective of the solid cell. Hence, when evaluating $\mathbf{F}^*$ in (27) for a solid cell at a solid/void boundary, the wave-processed states are taken as simply $u^* = u_{solid}$ and $p^* = 0$; i.e., the cell face is assumed to experience zero pressure and move at the velocity normal to the face interpolated from within the solid. Also, zero deviatoric

stress is applied at the solid/void boundaries in the construction of the strength flux, $\mathbf{F}_{stren_k}$ in (40). These two measures ensure that no work is done by the void particles on the solid and that no forces are applied. The modified Riemann problem solved between void and solid cells, from the perspective of the void cell, in order to meet criterion (iii), is described below.

The 'thermodynamic volume' of a computational particle is given by $V_{thermo} = \rho/m$ where ρ, m are the density and mass of the particle, respectively. The area of the corresponding cell (multiplied by unit length) gives a 'geometric volume' (V_{geom}), which is simply a function of the spatial distribution of particles in the domain and the definition of the Voronoi tessellation. Ideally one should have $V_{thermo} = V_{geom}$, but in practice this relationship is only approximately obeyed. The difference between the geometric and thermodynamic volume can be quantified by calculating a 'volumetric error,'

$$\text{volumetric error } (V_{ERR})\% = \frac{V_{geom} - V_{thermo}}{V_{thermo}} \times 100\%. \tag{46}$$

Experience has shown that solid particles at free surfaces are prone to develop significant values of V_{ERR} (volumetric errors of up to 40% have been noted in cells at free surfaces in shell collapse simulations where V_{ERR} was not controlled). Since free surfaces are defined by the position of the cell boundaries between solid and void particles, volumetric errors at free surfaces must be controlled if accurate predictions of free surface location are to be obtained. In addition, although V_{geom} is not explicitly used in our scheme, geometric errors imply errors in the cell side lengths S_k which have a direct impact on the magnitude of intercell fluxes. Moreover, volumetric errors for a solid cell at a free surface will change the aspect ratio of the cell and modify the influence of its cell-centred stress in Stage 2 of the deviatoric operator (see Section 3.4.2). The control of volumetric error essentially requires that the spacing between the solid particles and their void neighbours be regulated by the exertion of some correcting influence on the motion of the void particles. If a solid particle has a positive V_{ERR} (cell too large) then the neighbouring void particle needs to be moved closer, and vice versa. Provided this correction is applied only to void cells, no conservation error is introduced in the solid material.

The correction is achieved by a modification of the input states to the Riemann problem formed between void and solid cells when forming the hydrodynamic flux $\mathbf{F}_{hydro_k}$ from the perspective of the void cell. Essentially, void particles experience the cell face formed with the solid cell as a moving one-dimensional piston. Thus the input states at the boundary for the solid ($\rho_{solid}, u_{solid}, p_{solid}$) are specified as

$$\rho_{solid} = \rho_{void}, \quad u_{solid} = 2.0(u_{piston} + \delta u_{piston}) - u_{void}, \quad p_{solid} = p_{void}, \tag{47}$$

where $\rho_{void}, u_{void}, p_{void}$ are states interpolated to the boundary from within the void, u_{piston} is interpolated from within the solid, and u is taken as positive toward the solid. The quantity δu_{piston} represents an adjustment to the piston velocity which is used to control the volumetric error and is calculated as

$$\delta u_{piston} = H V_{ERR}, \quad H = C \times \frac{\text{characteristic cell dimension}}{\text{characteristic flow time}}, \tag{48}$$

where C is a constant to be selected by the user. In practice we have found that the solution is insensitive to the value of C over a wide range. For the beryllium shell problem

(see Section 4.2) H was taken as

$$H = 20 \times \frac{\text{typical cell diameter}}{\text{stopping time}}. \tag{49}$$

Using this method, the volumetric error at the shell surface was maintained at less than 1% throughout the simulation. It should also be noted that this technique does not specifically introduce any restriction on the size of the stable timestep for the overall scheme. The size of the stable timestep, however, can be controlled by particle pairs in the void regions as it can anywhere else in the calculation, since a flow calculation is still required in the void.

4. NUMERICAL EXAMPLES

4.1. Introduction

In order to illustrate the effectiveness of our technique, three simulations are presented. The first comprises the collapse of a cylindrical beryllium shell following initialisation with a radial velocity directed towards its centre. Next, the shock-capturing properties of the scheme are investigated by simulating wave structures generated during a moderate-velocity impact on a semi-infinite aluminium target. Finally, the large deformation capabilities of the scheme are investigated with the simulation of a high velocity impact. Material properties utilised in the three simulations are listed in Table I (here shock Hugoniot data is taken from [48]). Where appropriate, the results obtained using the technique are compared to those using the commercial AUTODYN-2D software. AUTODYN-2D [5] is a nonlinear transient dynamic analysis program which offers several solvers including both fixed-connectivity Lagrangian and meshless Lagrangian SPH solvers. Validation of our scheme is additionally obtained by comparing the shell collapse simulation with an analytical solution.

4.2. Collapse of Thick-Walled Cylindrical Beryllium Shell

This problem simulates the collapse of a cylindrical beryllium shell in a vacuum when subjected to an initial radial velocity directed towards its centre. As a consequence of radial convergence, the shell will thicken during collapse, and its kinetic energy is irreversibly converted to internal energy through the dissipative plastic distortion mechanism. The collapse terminates at a 'stopping radius,' which is a function of the initial conditions. This

TABLE I
Material Properties for Aluminium, Steel, and Beryllium

Property	Aluminium	Steel	Beryllium
Density, ρ (kgm^{-3})	2785	7900	1845
Bulk sound speed, c_0 (ms^{-1})	5328	4600	****[a]
Particle-shock velocity slope, S	1.338	1.490	1.124
Grüneisen parameter, γ	2.00	2.17	****[a]
Shear modulus, G (kPa)	2.760×10^7	8.530×10^7	15.100×10^7
Yield stress, Y_0 (kPa)	0.300×10^6	0.979×10^6	0.330×10^6

[a] **** denotes properties not required for the Osborne EOS. Additional parameters for the Osborne EOS can be found in the text.

problem presents an interesting challenge for a free-Lagrange hydrocode. Key criteria for a successful simulation are that (i) the computational mesh retains circumferential symmetry and (ii) the scheme accurately predicts the stopping radius. This problem is a modification of that of Verney [41] who experimentally studied the collapse of spherical uranium shells.

4.2.1. *Initialisation*

The shell is initially 20 mm thick with an internal radius of 80 mm. Relevant material properties for beryllium are listed in Table I. The Osborne EOS is used, with the following parameter values:

$$\begin{aligned} &a_1 = 0.951168, \quad a_2 = 0.345301, \quad a_2^* = -0.345301, \\ &b_0 = 0.926914, \quad b_1 = 2.948420, \quad b_2 = 0.507979, \\ &c_0 = 0.564362, \quad c_1 = 0.620422, \quad e_0 = 0.800000, \\ &\rho_0 = 1.845, \quad p_{min} = -0.10. \end{aligned}$$

Note that these parameters are given in the (gm, cm, μs) unit system and hence the calculated pressure is in units of Mbar and sound speed in units of cm/μs.

From a consideration of the governing equations in cylindrical coordinates, ignoring elastic effects and compressibility of the shell material, the initial radial velocity at the inner surface, u_0, required to produce an inner stopping radius of r_0' is (see the Appendix)

$$u_0 = \sqrt{\frac{2Y_0 F(\alpha, \lambda)}{\sqrt{3}\rho \ln(R_1/R_0)}}, \tag{50}$$

where R_0 and R_1 are the initial inner and outer radii and the function $F(\alpha, \lambda)$ has the form

$$F(\alpha, \lambda) = \int_\lambda^1 x \ln\left(1 + \frac{2\alpha + \alpha^2}{x^2}\right) dx, \tag{51}$$

where

$$\alpha = \frac{R_1 - R_0}{R_0}, \quad \lambda = r_0'/R_0, \quad x = r_0(t)/R_0, \tag{52}$$

and $r_0(t)$ is the dynamic inside radius. The numerical integration of the function $F(\alpha, \lambda)$, for a range of values of α, is shown in Fig. 2. Furthermore, the outer stopping radius r_1' can be related to the initial inner surface velocity via

$$F(z, \xi) = u_0^2 \frac{\sqrt{3}}{2} \frac{R_0^2}{R_1^2} \frac{\rho}{Y_0} \ln \frac{R_1}{R_0}, \tag{53}$$

where

$$F(z, \xi) = \int_\xi^1 z \ln\left(\frac{z^2 R_1^2}{R_0^2 - R_1^2 + z^2 R_1^2}\right) dz, \quad \xi = r_1'/R_1, \quad z = r_1(t)/R_1. \tag{54}$$

For the present shell configuration, $\alpha = 0.25$. Three simulations have been performed, with inner stopping radii selected as $r_0' = 50$, 45, and 40 mm, respectively. The initial velocity

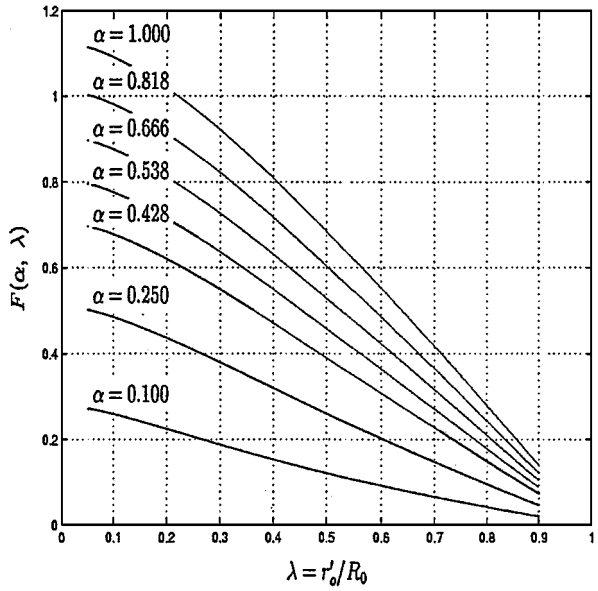

FIG. 2. Numerical integration of the function $F(\alpha, \lambda)$ for a variety of values of $\alpha = (R_1 - R_0)/R_0$. R_0 and R_1 are the initial inside and outside radii and r_0' is the inner stopping radius.

u_0 required at the shell inner face for these collapses, and the associated outer stopping radii, as predicted by the above analysis, is given in Table II. Each of the three shell collapse calculations were initialised by constructing a full 360-degree circumferentially symmetric distribution of both beryllium and void particles such that the initial Voronoi diagram provides the desired shell dimensions—see Fig. 5a. The stiffened gas EOS was chosen to describe the void particles, with material properties taken as those of aluminium—see Table I. Aluminium properties were chosen because aluminium has a lower compressibility than beryllium and hence the timestep is not excessively restricted by the central core of void particles as they are compressed by the collapsing shell.

Mesh resolution is the same for each collapse. The shell is represented by 20 rings of particles, equally spaced in the radial sense, each ring containing 256 particles. The mesh comprises a total of 13,937 particles, 8,817 of which fill the void regions. To initiate a collapse, the particles representing the shell are given an initial radial velocity $u(r)$ which, assuming incompressible flow, is obtained simply from

$$u_r = \frac{R_0}{r} u_0. \tag{55}$$

TABLE II
Theoretical Collapse Parameters for the Cylindrical Beryllium Shell, as a Function of the Inner Stopping Radius r_0'

r_0' (mm)	r_0'/R_0	$F(\alpha, \lambda)$	u_0 (ms^{-1})	$F(z, \xi)$	r_1' (mm)
50	0.6250	0.187946	417.1	0.120298	78.10
45	0.5625	0.223336	454.7	0.142933	75.00
40	0.5000	0.259727	490.2	0.166159	72.12

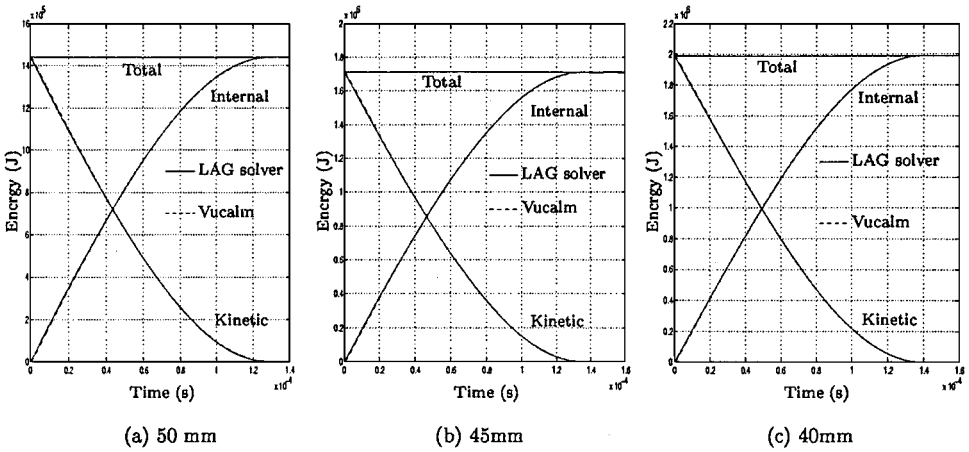

FIG. 3. Energy time histories for the three beryllium shell collapses: $r_0' = 50$, 45, and 40 mm. Shown are internal and kinetic energy histories for the free-Lagrange solver *Vucalm-EP* (dashed line) and the AUTODYN fixed-connectivity solver (solid line).

A CFL number of 0.4 is used in timestep control, and since the relative distortion of the material is low, the computational mesh is fully reconstructed on only 1 timestep in 10.

4.2.2. *Discussion*

For the three collapses the time histories of the energy distribution and of the inner, middle, and outer radii are plotted in Figs. 3 and 4, respectively. The inner and outer shell radii are calculated as an average of the vertex positions of the computational mesh on solid/void boundaries for the complete shell circumference. The middle radius r_m similarly tracks a material surface which is initially located at $R_m = (R_0 + R_1)/2$.

Figure 3 shows the nearly identical energy time histories for each collapse for both the free-Lagrange solver *Vucalm–EP* and the AUTODYN-2D fixed-connectivity Lagrangian solver. In each case the initial kinetic energy of the shell is converted into internal energy as irreversible plastic work is done. Total energy is accurately conserved in both schemes. In the early stages of the collapses the material distortion is purely plastic, but as a larger percentage of the initial kinetic energy is dissipated, portions of the shell enter the elastic regime. Eventually, an approximate state of rest is reached after which no further permanent plastic distortion occurs, but the shell maintains a small-amplitude elastic oscillation. This residual motion is not accounted for in the theoretical analysis, in which pure plastic behaviour has been assumed. Therefore, in order to compare the simulated shell behaviour with theory, the stopping time is taken as the period required for 99.9% of the initial kinetic energy to be converted to internal energy. Table III gives the stopping times for the simulations, together with the percentage errors for the inner and outer stopping radii relative to the theoretical values. Since the shell retains residual elastic motion the final stopping radii are taken as the median radii for the first elastic oscillation. The scheme is seen to match closely the theoretical stopping radii; agreement is to better than 1% in every case. From the limited range of the three cases investigated here, the difference between the simulated and theoretical radii appears to increase for the inner shell face and decrease for the outer as the severity of the collapse is increased.

Time histories for the shell radii are illustrated in Fig. 4 and are seen to be in close agreement with the AUTODYN-2D fixed-connectivity solver. Stopping times and deviations

TABLE III
Beryllium Shell Collapse Results for the Free-Lagrange Solver

Final radius r_0' (mm)	Initial kinetic energy (MJ)	Stopping time[a] (ms)	Inner radius error (%)[b]	Outer radius error (%)[b]
50	1.4401	127.8	−0.024	−0.662
45	1.7114	133.6	+0.267	−0.625
40	1.9891	137.0	+0.853	−0.571

[a] Stopping time is the time taken for the shell to dissipate 99.9% of its initial kinetic energy.
[b] Inner and outer radius errors are relative to incompressible theory.

from the incompressible theory are shown in Table IV for the fixed-connectivity solver. The recorded time for the shell to dissipate 99.9% of the initial kinetic energy is consistently longer with the free-Lagrange technique, ranging from an increase of 0.95% for the 40-mm collapse to 1.64% for the 50-mm collapse. Differences between the stopping radii and the theoretical prediction are generally smaller than they are for the free-Lagrange solver. The maximum deviation from the incompressible theory for the inside and outside radii were recorded for the 40-mm collapse as 0.090% and 0.025%, respectively.

Table V compares the stopping radii for the two numerical techniques. Also included are data characterising the degree of circumferential symmetry achieved by the free-Lagrange solver at the end of the collapse. These data include the standard deviation of the normalised particle radius σ, which is determined as follows. First a mean radius $\overline{r}^n$ is calculated for each of the 20 circumferential rings $n = 1, \ldots, N$,

$$\overline{r}^n = \frac{1}{I}\sum_{i=1}^{I} r_i^n, \quad I = 256, \quad N = 20, \tag{56}$$

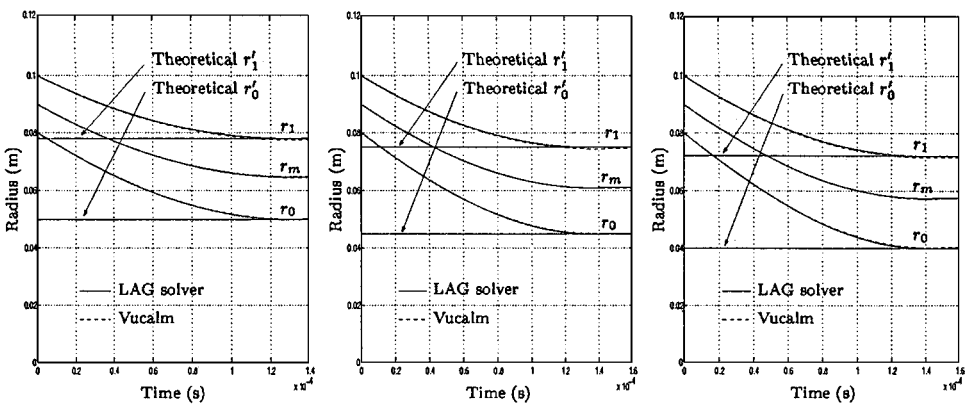

FIG. 4. Radius time histories for the three beryllium shell collapses ($r_0' = 50$, 45, and 40 mm) for the free-Lagrange solver *Vucalm-EP* (dashed line) and the AUTODYN fixed-connectivity solver (solid line). r_0, r_1, and r_m are the inner, outer, and middle radii, respectively. Also shown are the inner and outer stopping radii obtained from incompressible theory.

TABLE IV
Beryllium Shell Collapse Results for the AUTODYN-2D Fixed-Connectivity Lagrangian Solver

Stopping radius r_0' (mm)	Stopping time[a] (ms)	Inner radius error (%)[b]	Outer radius error (%)[b]
50	125.7	+0.066	+0.023
45	131.4	+0.050	+0.018
40	135.7	+0.090	+0.025

[a] Stopping time is the time taken for the shell to dissipate 99.9% of its initial kinetic energy.

[b] Inner and outer radius errors are relative to incompressible theory.

where r_i^n is the radial position of an individual computational particle in the shell. Normalising with respect to this mean radius for each ring, the standard deviation for the particle radii is calculated,

$$\sigma(\%) = \sqrt{\frac{1}{N \times I} \sum_{i=1}^{I} \sum_{n=1}^{N} \left(\tilde{r}_i^n - 1\right)^2} \times 100\%, \quad \tilde{r}_i^n = \frac{r_i^n}{\bar{r}^n}. \tag{57}$$

In addition, the minimum and maximum deviations from the mean radii are quoted for any particle in the shell.

Agreement of the inner and outer stopping radii between the free-Lagrange and AUTODYN-2D fixed-connectivity solvers is excellent: no difference exceeds 0.8%. The preservation of circumferential symmetry, evident in the final mesh configurations illustrated in Figs. 5b, c, and d, is quantified by the standard deviation of the normalised particle radius, which reaches a maximum of 0.038% for the 45-mm collapse. The maximum and minimum deviations from the mean radii are perhaps more informative. As one might expect, the minimum and maximum deviations increase in magnitude as the final stopping radius decreases, i.e., as the distance travelled by the computational particles increases. In conclusion, the free-Lagrange simulation meets our two key criteria for this test problem: circumferential symmetry is preserved, and the stopping radii are accurately predicted.

TABLE V
Beryllium Shell Collapse[a]

Inner stopping radius, r_0' (mm)	Inner radius difference (%)	Middle radius difference (%)	Outer radius difference (%)	Standard deviation σ (%)	Minimum deviation (%)	Maximum deviation (%)
50	−0.090	−0.358	−0.685	0.0303	−0.0923	+0.1004
45	+0.244	−0.231	−0.643	0.0379	−0.1172	+0.1213
40	+0.762	−0.056	−0.596	0.0365	−0.1381	+0.1422

[a] Listed are comparisons for inner, middle, and outer stopping radii between the free-Lagrange and AUTODYN-2D fixed-connectivity solvers. Also shown, as a measure of radial symmetry for the free-Lagrange simulations, are standard deviations of a normalised particle radius, and minimum and maximum deviations from that radius—see text.

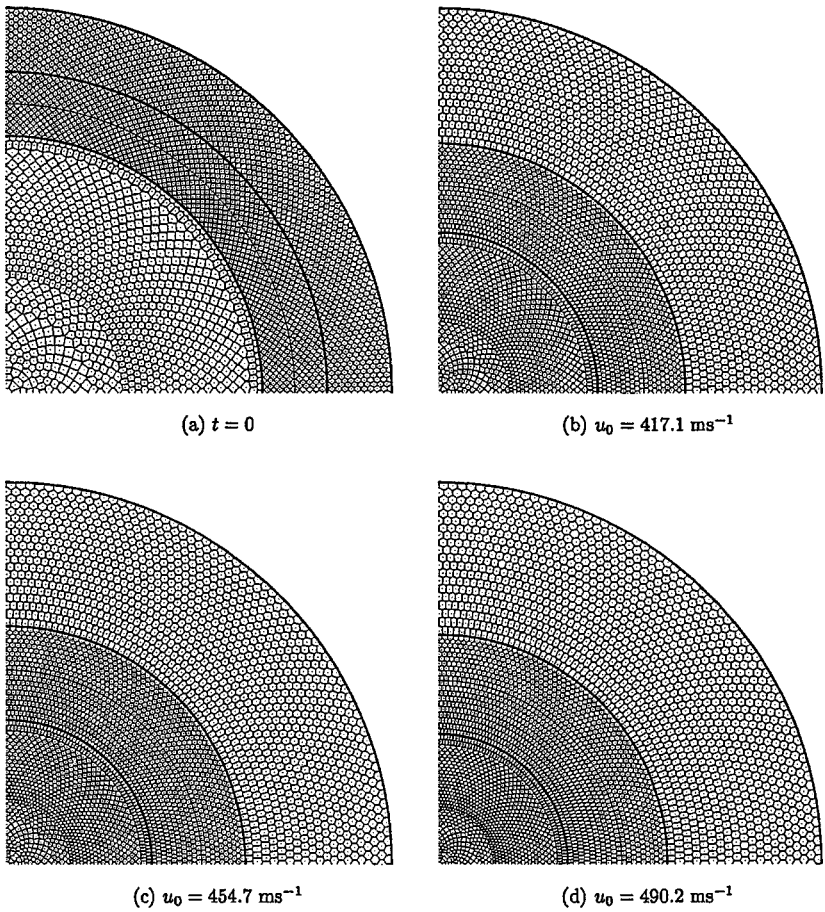

FIG. 5. Computational mesh configurations for free-running beryllium shell collapse: (a) initial mesh configuration for the three test collapses; (b)–(d) meshes after collapses for stopping radii of 50, 45, and 40 mm, respectively.

4.3. Low-Velocity Projectile Impact

In this problem, an aluminium projectile strikes a semi-infinite aluminium target in vacuo with an initial velocity of 400 ms^{-1}. The stiffened gas EOS is used, together with material properties as given in Table I. The problem has been previously investigated by Tyndall [40] using a FCT-based scheme on a stationary Eulerian mesh and employing the volume-of-fluid (VOF) method to track material interfaces.

4.3.1. *Initialisation*

Figure 6 shows the initial configuration of the problem. Target and projectile dimensions are $2.20 \times 10^{-2} \times 3.80 \times 10^{-2}$ m and $0.50 \times 10^{-2} \times 1.20 \times 10^{-2}$ m, respectively. The target and projectile are enclosed within a global computational domain $3.00 \times 10^{-2} \times 4.00 \times 10^{-2}$ m and are surrounded by void particles to enable unrestricted free surface motion. As in the preceding problem, the void particles are modelled using the stiffened gas EOS and are assigned the properties of aluminium.

Simulations are performed at five levels of mesh resolution in order to study the convergence of the scheme. Initial particle spacings in the x- and y-directions are the same

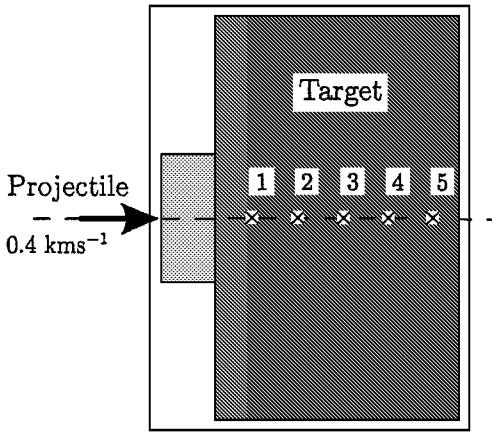

FIG. 6. Computational domain for low-velocity impact simulation. Shown are a projectile with initial velocity 400 ms^{-1}, and a semi-infinite aluminium target containing Lagrangian reference points 1–5 (see text).

at each level of resolution, i.e., $\Delta x = \Delta y$. Data for the five computations are given in Table VI. Note that the tabulated number of particles includes the void particles. Relative execution times, calculated from the average of three runs, are included to indicate respective CPU cost. Also shown is the number of timesteps which are executed before the computational mesh is fully reconstructed, N_{recon} (see Section 3.1). Since the size of the stable timestep decreases with increased mesh resolution, distorton of the computational mesh, per timestep, lessens for increasing resolution, and hence the maximum value of N_{recon} that can be safely employed increases as the mesh is refined. Increasing N_{recon} reduces the CPU usage per timestep; hence the quoted execution times are an indication of the relative expense of each level of refinement when executed under conditions of best practice.

The problem is executed to an elapsed time of 3.0 μs after initialisation and a CFL number of 0.3 is used throughout. Actual computation time for the coarsest mesh (4800 particles) is approximately 210 s on a Pentium III 450-MHz processor.

TABLE VI

Particle Distributions, Mesh Reconstruction Details, and Relative Execution Times for the Low-Velocity Projectile Impact Simulation

Number of particles	N_{recon}	Relative execution times
4800 (60 × 80)	1	1.00
19200 (120 × 160)	3	4.7
30000 (150 × 200)	5	8.1
76800 (240 × 320)	8	32.3
120000 (300 × 400)	10	64.1

[a] Five levels of mesh resolution are used to study scheme convergence with initial mesh resolution identical in both x- and y-directions. N_{recon} is the number of timesteps executed before the computational mesh is fully reconstructed.

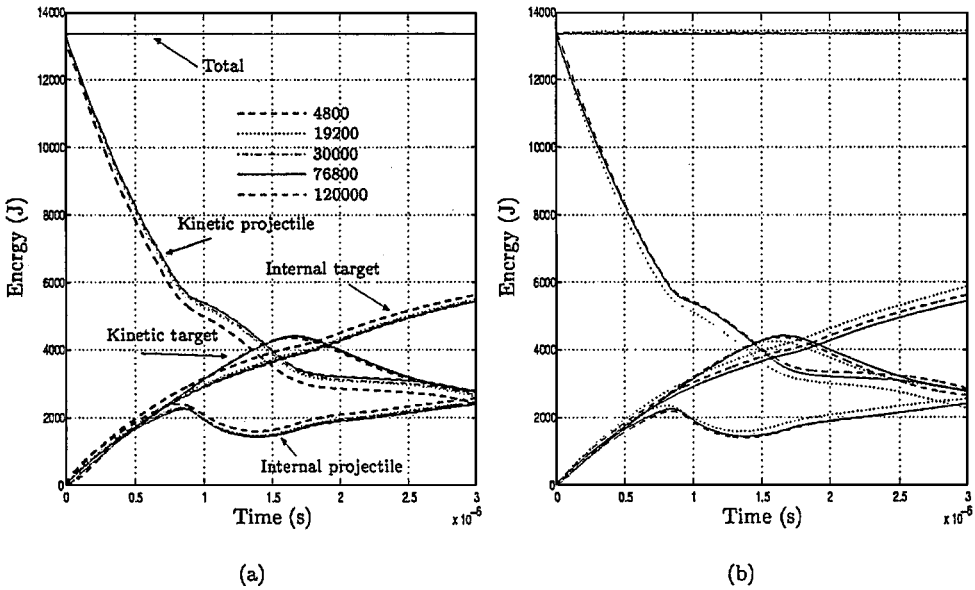

FIG. 7. Energy time histories for low-velocity impact simulation, depicting kinetic energy and internal energy for both the projectile and the target, plus system total energy. (a) Energy histories at differing levels of particle refinement-numbers indicate total particles in calculation. (b) Comparison between the free-Lagrange solution (solid line—76,800 particles, CFL $= 0.3$, $N_{recon} = 5$) and that obtained using the AUTODYN fixed-connectivity Lagrangian (dashed line) and SPH (dotted line) solvers.

4.3.2. *Discussion*

Convergence of the scheme under refinement is gauged by comparing the energy time histories at each of the five resolution levels; see Fig. 7a. Shown are the internal and kinetic energies for both the projectile and the target, plus the total energy of the system. The minimum in the projectile internal energy, which occurs after approximately 1.35 μs, provides a convenient point of comparison. On refining from 4,800 to 19,200 particles, the change in internal energy seen, at this minimum is just over twice the corresponding change between the 19,200 and the 76,800 particle meshes. This is consistent with first-order convergence. Visual inspection of the curves shows similar convergence behaviour throughout the calculation. The change in energy levels between the two finest meshes is typically less than 0.5%. Therefore, for the purpose of comparison with the other solvers, the level of convergence obtained with 240×320 particles is deemed adequate. Fig. 7b compares the energy histories of the AUTODYN fixed-connectivity and SPH solvers with that of the free-Lagrange solver. Agreement among the three techniques is generally close and it is evident that out of the four schemes the *Vucalm–EP* solver most accurately conserves total energy. The total energy differs from the initial kinetic energy of the projectile (the only energy present at $t = 0$) at the termination of the calculation ($t = 3.0$ μs) by 0.0052% for the *Vucalm–EP* solver compared with 0.52% for the Euler, 1.11% for the fixed-connectivity, and 0.69% for the SPH solver.

Figure 8 illustrates the wave structures generated in the projectile and target at 0.5, 1.0, 2.0, and 3.0 μs after problem initialisation. At 0.5 μs, shock waves, generated at the impact plane, are seen to propagate leftward, back into the projectile, and rightward into the target. Since the impactors share common material properties, these waves are identical

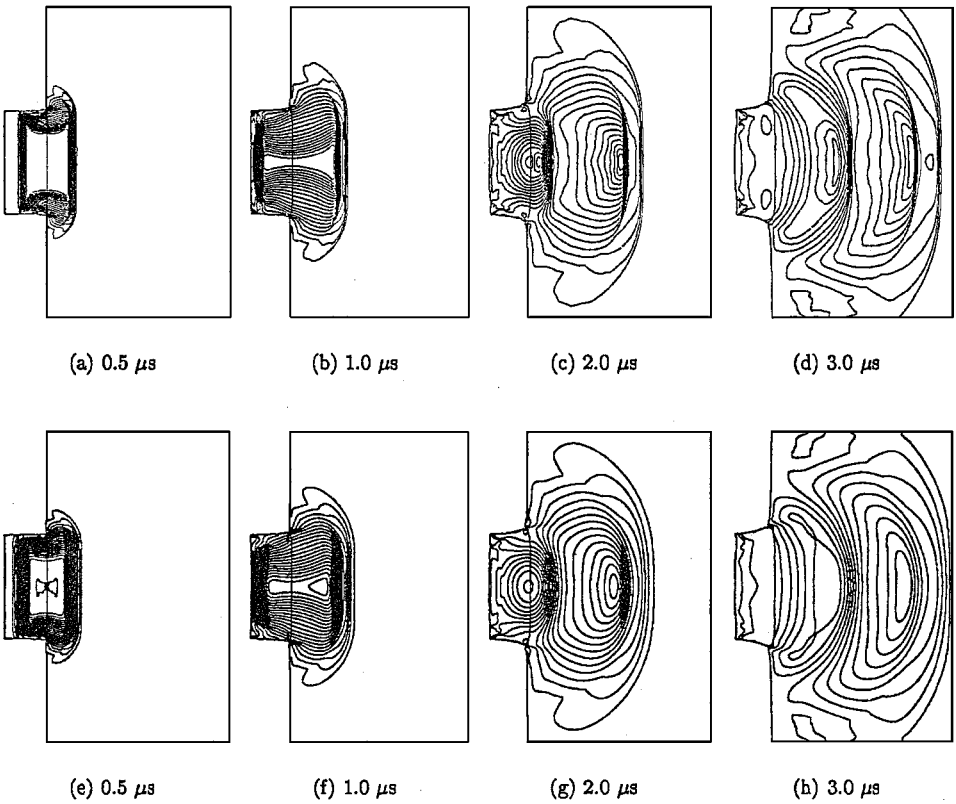

FIG. 8. Transient results from low-velocity impact at elapsed times of 0.5, 1.0, 2.0, and 3.0 μs after initial projectile impact (76,800 particles, CFL $= 0.3$, $N_{recon} = 5$). Shown are the material interfaces and contours of total x-wise stress σ_x with a contouring interval of 0.15×10^6 kPa. Panels (a) to (d) show the solution from the scheme in normal operation and (e) to (h) display the solution when piecewise-constant data reconstruction is used.

along the axis of symmetry. By 1.0 μs, rarefaction waves, which originate from shock reflection at the upper and lower free surfaces of the projectile, are about to meet at the symmetry axis. The left-running shock wave has also reached the rear of the projectile and has reflected as a rarefaction. The ability of the technique to model elastic–plastic response is evident in the splitting of the right-running shock wave at this time. After 2.0 μs, the two-wave family has matured and an elastic precursor wave and trailing plastic shock have formed. The rarefaction returned from the rear of the projectile has now crossed into the target, producing a region of high tensile stress in the x-direction (a maximum of approximately -1.9×10^6 kPa). At the final elapsed time of 3.0 μs, wave structures have reached the top and bottom of the target, and the plastic shock is beginning to weaken due to the interaction with trailing rarefactions. Deformation of the impactors is visible at the impact plane, and at the rear and top and bottom of the projectile. By performing calculations in which the first derivatives of the primitive variables (ρ, u, v, p) and the stress gradients (see (37)) within individual computational cells are set equal to zero, it can be shown that the scheme benefits from linear data reconstruction. Figures 8e to 8h illustrate the solution when such piecewise-constant data reconstruction is used. In this first-order solution the wave structures are distinctly more diffuse than in the solution obtained using

the MUSCL formed gradients. Calculation of the observed order of the scheme under mesh refinement, via the evaluation of a grid convergence index (GCI), as advocated by Roache [29], has also indicated local convergence which was never below order 1.4 [17] for this problem.

A consideration of the evolution of this simulation uncovers a limitation in the free-Lagrange solver as currently configured. When two materials come into contact, the solver considers them to be merged with infinite friction. In practice, for such a low-velocity impact, this is physically unrealistic since no tensile force would exist between the projectile and target in the x-direction, i.e., the impactors would not become physically fused together. Lagrangian slidelines or contact logic, used in traditional fixed-connectivity Lagrangian solvers, would correctly model this. Note that in the calculations performed using the AUTODYN fixed-connectivity solver, this feature was disabled in order to permit direct comparison with the free-Lagrange results. Since our scheme calculates the direct and shear stress, s_{nn_k} and s_{tt_k}, acting on each cell face, a number of physically more realistic material models could, however, be incorporated in the future. For instance, if at material interfaces, s_{tt_k} was set to zero and s_{nn_k} was limited to negative values (positive directed out of cell) in the deviatoric operator, and p^* was limited to positive values in the hydrodynamic operator, then this would result in a zero friction interface unable to support tension. More challenging, however, would be to enable such interfaces to separate, as this would require the creation of void particles at the interface as separation occurred. Similar considerations would be required to model fracture and spallation. This issue will be the subject of future work.

In order to further compare the solution obtained using the free-Lagrange solver with both the AUTODYN-2D fixed-connectivity and the SPH solver, five Lagrangian reference points are defined along the symmetry axis within the target (Fig. 6). Point 1 is initially 1.8125 mm from the impact plane, and the point spacing is 3.6250 mm. Figure 9 shows the time histories of x-wise velocity, pressure, density, and total stress in the x-direction, recorded at these points, for the free-Lagrange and AUTODYN fixed-connectivity solvers. The arrival times and amplitudes of the various wave systems are generally in good agreement at all points. Shock resolution is comparable, yet there is some disagreement in the values of pressure (2.4%) and density (2.1%) reached behind the first shock as recorded at point 1. This also has an impact (1.6%) on the total x-wise stress attained since $\sigma_x = -p + s_x$. It is suspected that this is caused by slight differences in the EOS used in the two solvers for this problem. The Mie–Grüneisen EOS, utilising a linear shock Hugoniot as the reference curve, was used in the AUTODYN solver, while the stiffened gas EOS was used in the free-Lagrange solver. The evolution of the right-running composite shock wave is clearly revealed in the time histories. At point 1, only a single incident shock is seen. At point 2, the shock front shows a break in slope, which is the first indication of shock splitting. At points 3 to 5 the elastic and plastic waves are distinct, with the elastic precursor increasingly separated from the plastic shock. Note that both the elastic and plastic waves remain steep and well resolved in the free-Lagrange calculation, while the fixed-connectivity solver suffers some diffusion and loss of wave steepness as the wave system propagates from points 1 to 5.

Figure 10 shows a similar comparison for the AUTODYN SPH and free-Lagrange solvers. Again the two techniques show good agreement for the arrival times and amplitudes of the right-running compression wave and the reflected rarefaction. As one may expect, the SPH solution is considerably more diffuse.

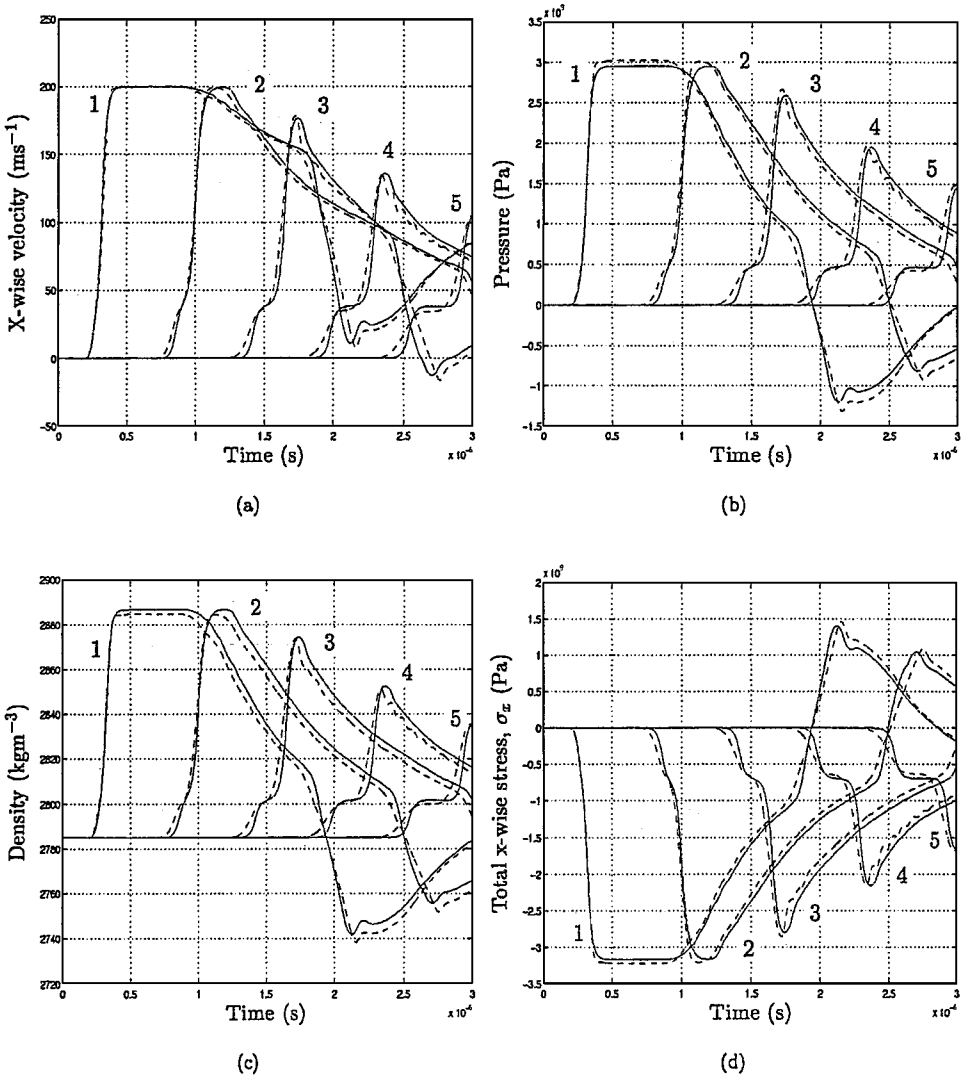

FIG. 9. Time histories for low-velocity impact simulation, recorded at Lagrangian reference points 1 to 5 within the target (see Fig. 6). Solid line is solution obtained using the free-Lagrange technique (76,800 particles, CFL $=$ 0.3, $N_{recon} = 5$); dashed line depicts solution obtained using the AUTODYN fixed-connectivity Lagrangian solver.

4.4. High-Velocity Impact Simulations

For the final numerical examples, simulations of high-velocity (3.1 km^{-1}) aluminium and steel projectiles impacting a thin aluminium target are presented. Following the categorisation proposed by Swift [32] and Zukas [47], the impact velocity lies somewhere between high and hypervelocity for the structural metals aluminium and steel. Thus we would expect to observe a highly localised fluid-like plastic response, since the pressures generated by the impact will be orders of magnitude greater than the yield strength of the material. The problem is dominated by inertia, is momentum driven, and would undoubtedly feature material failure. Because of the large and highly localised deformation common in this type of problem, simulations using conventional hydrocodes would normally be restricted to Eulerian schemes or to SPH.

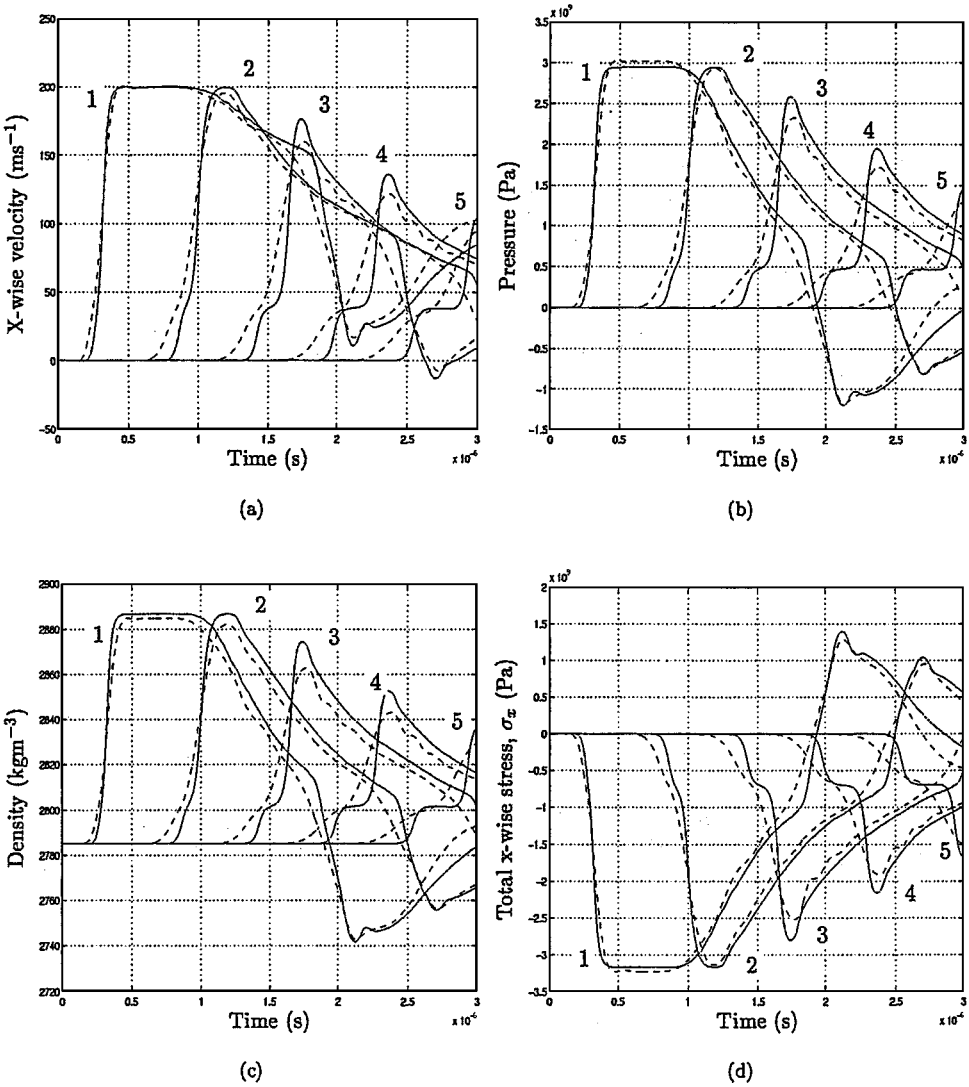

FIG. 10. Time histories for low-velocity impact simulation, recorded at Lagrangian reference points 1 to 5 within the target (see Fig. 6). Solid line is solution obtained using the free-Lagrange technique (76,800 particles, CFL $= 0.3$, $N_{recon} = 5$); dashed line depicts solution obtained using the AUTODYN Lagrangian SPH solver.

4.4.1. *Initialisation*

The computational domain employed in this simulation is shown in Fig. 11. The initial particle distribution, which completely fills the domain, is constructed from a number of elements. A circumferentially symmetric distribution consisting of 4,505 particles is used to discretise the circular projectile, which is 10 mm in diameter. Rectilinear particle distributions are used elsewhere to form the rectangular target (2×50 mm) and the majority of the void region. The void region must be relatively large in order to provide sufficient space to accommodate the anticipated large-scale deformation of the target and projectile. The total number of particles initially within the domain is 36,275, 2,500 of which are used in the target. Therefore, only approximately $1/5$ of the total computational particles constitute materials of interest. Fine distributions of void particles are used close to the

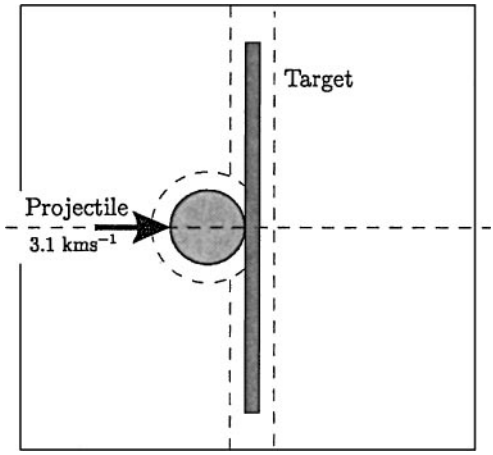

FIG. 11. Domain configuration for the high-velocity impact of aluminium and steel projectiles on a thin aluminium target. Dashed lines enclose regions of fine particle distribution. The aperture in the left boundary admits void particles throughout the calculation.

projectile and target (indicated by the dashed lines in Fig. 11), and coarser distributions are used in the remainder of the domain to help reduce computational cost. Throughout the duration of the calculation, additional void particles are added through an aperture in the left-hand boundary, at the impact velocity, to maintain the integrity of the computational mesh. Again the stiffened gas EOS is used for both steel and aluminium (see Table I for material properties). A CFL number of 0.3 is used in timestep control, and the mesh is fully reconstructed every 3 timesteps. The solutions are compared with results from the AUTODYN SPH solver. Since no void regions are required for the SPH solver, only a discretisation of the target and projectile using SPH nodes is necessary.

4.4.2. *Discussion*

Transient results to an elapsed time of 8.0 μs from initial impact are shown in Fig. 12 for an aluminium projectile striking an aluminium target. Figures 12a–12h show the material geometry and pressure distributions predicted by the free-Lagrange solver, while Figs. 12i–12p show node locations for the comparable AUTODYN SPH solution. As expected, the massive compression generated by the impact produces extreme pressures. After 1.0 μs (Fig. 12a), a shock wave is seen running leftward into the projectile closely followed by the rarefaction formed at the rear face of the target. Here all shocks are 'overdriven' and hence no split elastic/plastic wave structures are observed. The pressure at the centre of the projectile, behind the leftward running shock, is recorded as 18.6×10^6 kPa. Figure 13 shows part of the free-Lagrange computational mesh in the vicinity of the projectile at 1.0 μs. Even at this early time, Lagrangian motion of the mesh, and the formation of ejecta from both the projectile and target, is evident. Considerable deformation of both projectile and target is seen at 2.0 μs (Fig. 12b), with thin arms of ejecta released from the front face of the target. Reflection of the focused wave structures at the rear face of the projectile, observable in Figs. 12b and 12c, produces a region of strong tension. A tensile pressure of -15.9×10^6 kPa is noted in the core of the wave structure. With a more realistic material model, failure by spallation would be expected here. By 4.0 μs, the majority of this wave has reflected as a compression

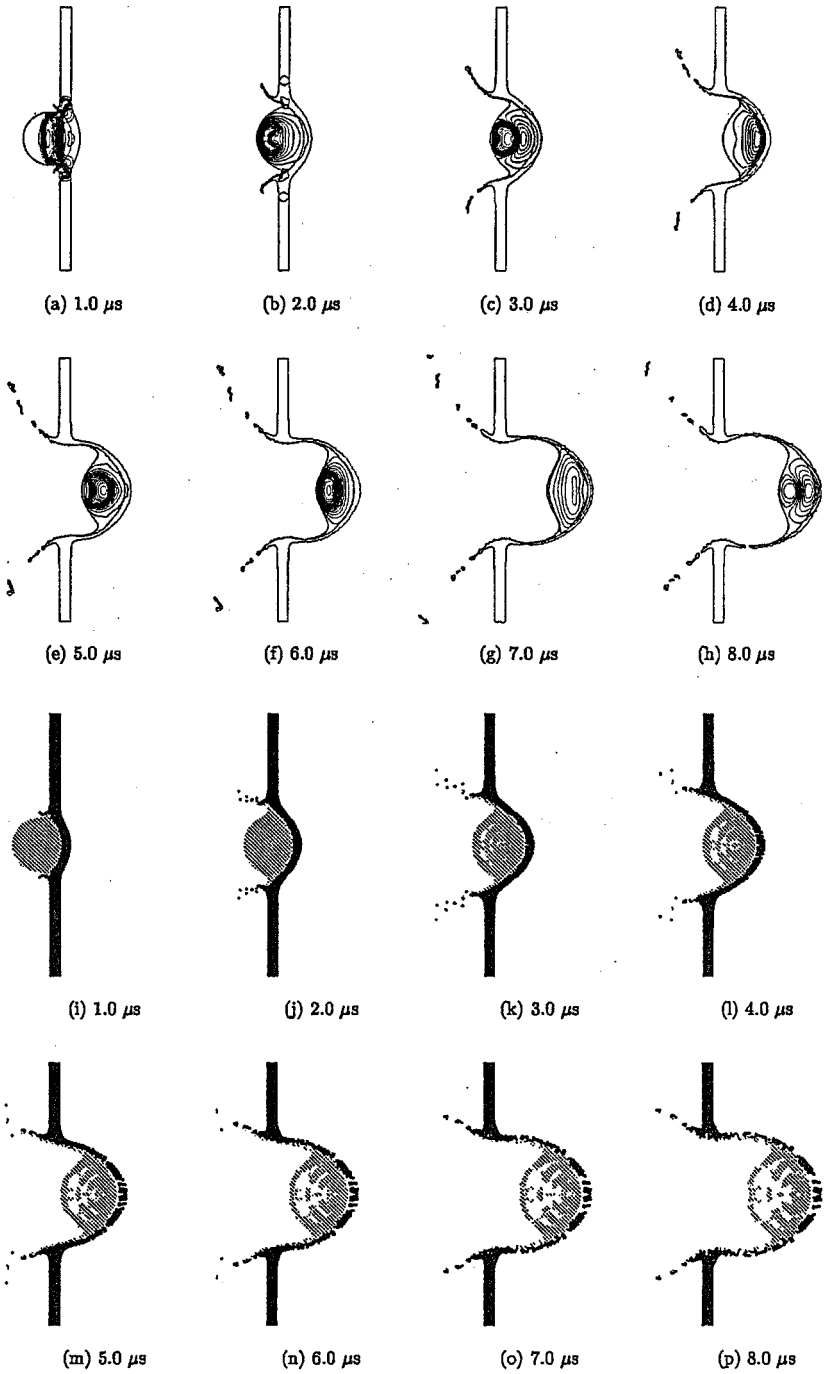

FIG. 12. Transient results illustrating material deformation and wave structures for the high-velocity impact of a circular aluminum projectile on an aluminium target. (a)–(h) free-Lagrange solution—plotted are material interfaces plus pressure contours with a contour interval of 1.0×10^6 kPa. (i)–(p) SPH solution—black and grey points are SPH nodes in the target and projectile, respectively.

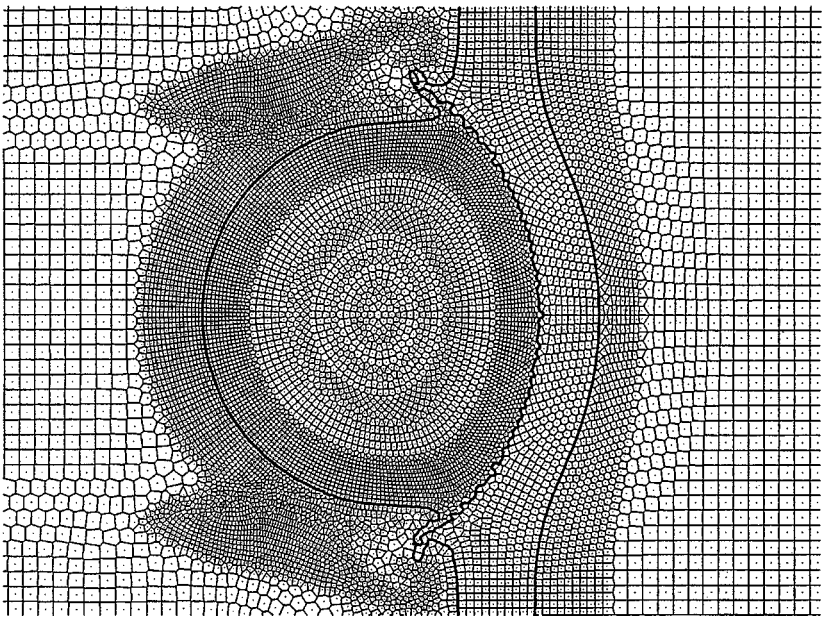

FIG. 13. Detail of free-Lagrange computational mesh for the high-velocity impact simulation, aluminium projectile and target, at 1.0 μs. Heavy lines are free surfaces.

front and is crossing the boundary from the projectile into the now highly deformed target. Regions of ejecta have begun to break away from the front of the target and continue at high velocity into the void regions. By 7.0 μs, the projectile penetrates the target to such an extent that the narrow remaining regions of the target present little resistance and the target has only marginal influence on the momentum of the projectile. At later times, the target material ligaments above and below the projectile are stretched and narrowed until they are represented by only a single row of particles, at which stage the material typically fails due to 'numerical fragmentation.' This occurs when the particles representing the ligament move sufficiently far apart that, upon mesh reconstruction, adjacent particles cease to be connected. Hence tensile forces can no longer be transferred through the ligament. At this point fragmentation occurs and void particles begin to fill the gap. Such numerical fragmentation is evident in the ejecta and the highly deformed target in Fig. 12h.

The SPH results (Figs. 12i–12p) show deformations at each time that agree closely with the free-Lagrange solution. Slight differences develop as the calculation proceeds due to the numerical characteristics of each of the two schemes. For instance, the SPH method is well known for displaying an instability in tension. As a consequence, the region subjected to large tensile forces, in the rear of the projectile, exhibits a 'numerical fracture' at 2.0 μs, forming a void in the projectile. This void persists and continues to grow for the remainder of the calculation. The presence of the void enlarges the projectile such that it extends over a thickness of approximately 11.6 mm in the x-direction after 8.0 μs compared to approximately 6.8 mm, as illustrated in Fig. 12h. Despite these differences, the final configurations are very similar for both schemes. The progress of the projectile through the target is approximately 20.5 mm for the free-Lagrange solver, compared with 21.9 mm obtained using SPH, while the widths of the holes produced in the target are approximately 19.2 mm and 20.5 mm, respectively.

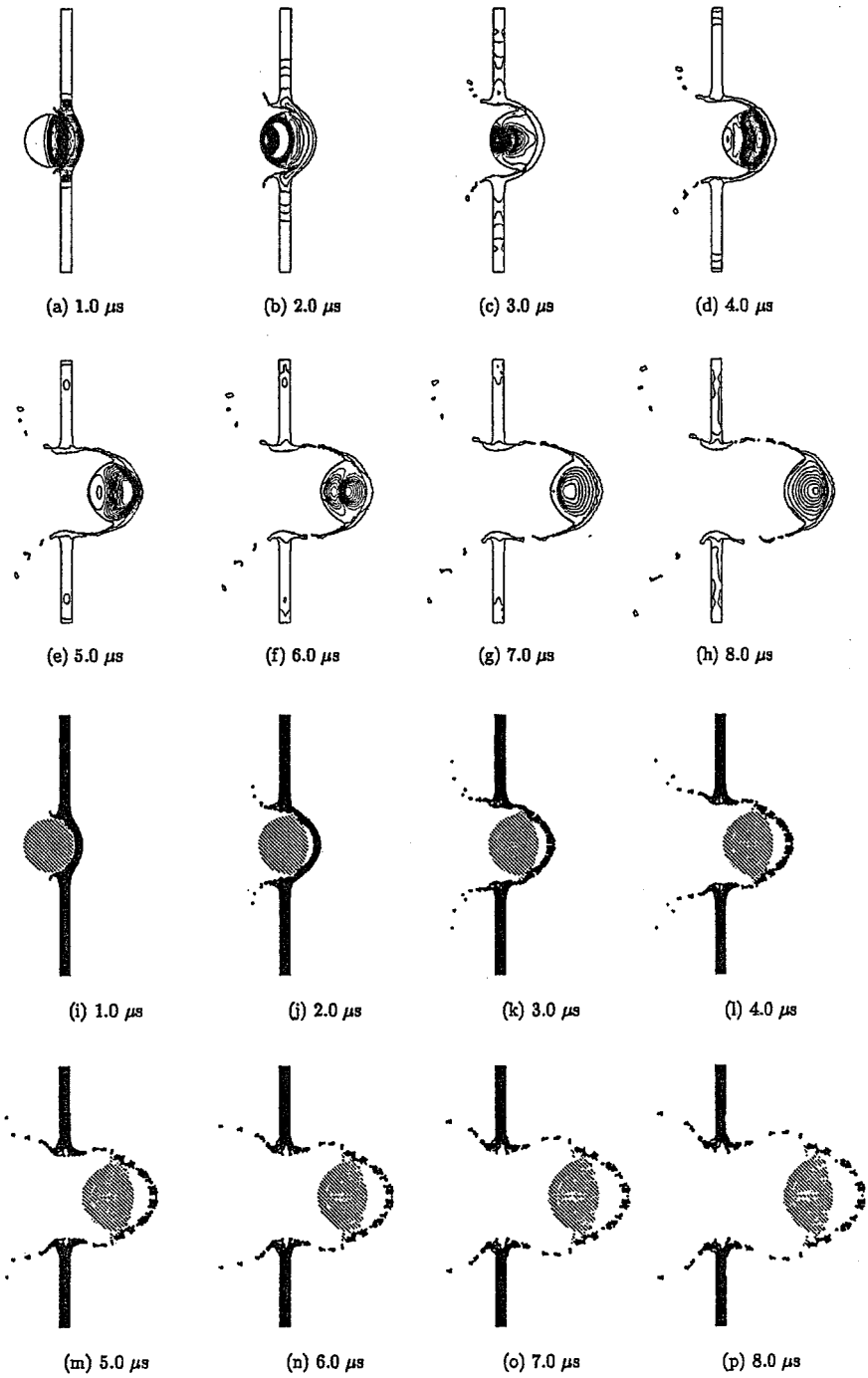

FIG. 14. Transient results illustrating material deformation and wave structures for the high-velocity impact of a circular steel projectile on an aluminium target. (a)–(h) Free-Lagrange solution—plotted are material interfaces plus pressure contours with a contour interval of 1.0×10^6 kPa. (i)–(P) SPH solution—black and grey points are SPH nodes in the target and projectile, respectively.

A second high-velocity impact simulation was performed in which all parameters are unchanged, with the exception that the projectile is constructed from steel. Transient solutions for the simulation, performed using both free-Lagrange and SPH, are shown in Fig. 14. Since the steel projectile is more massive and so possesses significantly more initial kinetic energy, the compression on impact is more severe than for the aluminium/aluminium problem. At 1.0 μs, a maximum pressure of approximately 27.9×10^6 kPa is generated within the projectile behind the left-running shock wave. Also, as there is now an impedance mismatch at the interface between the projectile and target, the rarefaction produced at the rear of the target is not fully transmitted into the projectile. Instead, a proportion of the rarefaction is reflected back into the target as a weak expansion wave. This produces a minimum pressure of -9.5×10^6 kPa and total tensile x-wise stress of -9.9×10^6 kPa at the interface between the steel and aluminium. As in the aluminium/aluminium simulation, the free-Lagrange scheme resolves a number of complex wave interactions. In the steel/aluminium case, shock focussing within the projectile produces a high pressure 'core' which is apparent from 3.0 μs onward, while the region of high tensile stress seen at the rear of the projectile in the aluminium/aluminium case is now absent. A maximum pressure of 27.2×10^6 kPa (close to that produced upon initial impact) is recorded very near the rear of the projectile. After 4.0 μs (Fig. 14d), the projectile has made marginally more progress through the target compared with the aluminium/aluminium solution. The deformation of the projectile is also considerably less due to the increased yield stress of the steel. The amount of ejecta formed is also significantly reduced. In the aluminium/aluminium simulation, roughly equal quantities of projectile and target material were ejected from the front of the target. However, since the steel projectile is more resistant to deformation, no steel is released to form ejecta. Furthermore, the projectile 'plugs' the target, retaining a larger proportion of the target material on the front half of the projectile. This decreases the amount of material available to form ligaments above and below the projectile. Consequently, the ligaments are thinner and suffer earlier numerical fragmentation than in the aluminium/aluminium simulations (see Fig. 14f).

Results obtained for the steel/aluminium problem using SPH are illustrated in Figs. 14i to 14p. As in the aluminium/aluminium simulation, the SPH solution closely matches the free-Lagrange results at early times. The solutions begin to differ noticeably at 2.0 to 3.0 μs, when the SPH simulation undergoes numerical fracture at the projectile/target interface as a result of large local tensile forces, forming a void between the projectile and target. This is a numerical artifact similar to the fracture at the rear of the projectile in the aluminium/aluminium case, the different location of the failure reflecting the changed stress distribution. However, the absence of high tensile stress in the bulk of the steel projectile means that it remains intact, and despite the formation of the void between the projectile and target, the projectile deformation very closely matches that predicted by the free-Lagrange solver. At 8.0 μs, the progress of the projectile through the target agrees almost exactly (approximately 22.8 mm for both methods) while the target hole is marginally larger for SPH (16.4 mm as against 15.7 mm).

In both the free-Lagrange and SPH simulations presented here, 'penetration' problems, as reported by Monaghan [24] and commonly observed in particle methods, do not appear to be of concern. The authors have previously investigated the problem of mesh-induced penetration errors at material interfaces in free-Lagrange simulations of gas-phase Richtmyer–Meshkov instability [18]. Because material interfaces always lie along cell boundaries in our scheme, the interfaces are typically slightly wrinkled at the length scale of the mesh

pitch. If the interface is unstable, then such wrinkles introduce high-wavenumber perturbations to the interface, which can grow to contaminate the solution. In [18] we introduced a simple interface smoothing algorithm to damp out such perturbations. However, in the present work the smoothing algorithm was found to be unnecessary and has not been used. Although the presence of material strength may be expected to inhibit the growth of interface instabilities, we also repeated several cases without material strength and found that the interfaces remained well behaved. It is the authors' opinion that in the simulations presented here, particularly the high-velocity impact, penetration problems are not observed at material interfaces either because the interface is not particularly unstable or because the time scale of the simulation is much shorter than the development time of any instability.

5. CONCLUDING REMARKS

We have presented a conservative, two-dimensional numerical scheme which models elastic–perfectly plastic solids using planar geometry, in the Lagrangian reference frame. By decomposing the total stress tensor into a hydrostatic pressure and deviatoric stress component, the governing equations can be solved sequentially in time using a time-operator split technique. A hydrodynamic operator, based on a second-order, finite-volume Godunov method is used to advance the conserved variables to an intermediate time level. Next, a separate deviatoric operator calculates a new stress state, based on these intermediate values, in order to provide a final conservative update. Since the scheme is fully Lagrangian, material interfaces are sharply resolved at all times and multimaterial problems can be represented easily-no additional algorithms are required to track material interfaces. Riemann problems, formed at the boundaries between individual computational cells, are solved using an approximate two-shock solver to obtain Godunov fluxes, and materials are characterised solely by a linear approximation to the shock Hugoniot and the local sound speed. Therefore, a broad range of materials can be simulated including fluids (the techniques discussed in this paper have previously been employed to simulate the collapse of air cavities in water [3]) and condensed materials. In high-distortion calculations, the tangling of conventional fixed-connectivity Lagrangian meshes is avoided by utilising the free-Lagrange method. All variables are considered to be 'cell-centred,' being stored at computational particles which are the only permanent feature of a calculation.

To illustrate the characteristics of the scheme, a variety of numerical examples were presented. The first simulated the collapse of a cylindrical elastic–plastic shell. For a range of moderately severe collapses the scheme maintained a high degree of circumferential symmetry and reproduced an analytical stopping radius, obtained from an incompressible model, consistently within 1%. Simulations of the shell collapse also agreed closely with those performed using a conventional fixed-connectivity solver. The shock-capturing properties of the scheme were investigated and compared with those of a fixed-connectivity and SPH solver by simulating a low-velocity impact problem. The scheme was found to diffuse shock waves less than the other solvers and to converge at first-order or better under mesh refinement. By simulating a high-velocity impact, it was also demonstrated that the scheme is capable of computing arbitrarily large material deformations. The computational cost of the method is found to be significantly more than that of fixed-connectivity and SPH solvers. The computational efficiency of the technique suffers somewhat due to the necessity of using void particles in vacuum regions and to the requirement to perform frequent mesh reconstructions.

The authors believe, however, that the proposed technique provides a sound foundation for more advanced material modelling and the incorporation of more realistic physics. By avoiding the complexities of incorporating material strength within the Riemann problem, behaviour such as work hardening can be easily included. For example, the constant yield strength utilised in the definition of the yield condition can be made a function of the equivalent strain recorded at individual particles. Such refinements will be the subject of future work.

APPENDIX: THEORETICAL CYLINDRICAL COLLAPSE MODEL

In this section, the theoretical collapse of a spherical shell, as presented by Verney [41], is reworked for the case of a cylindrical shell. The objective is to find an initial velocity distribution necessary to symmetrically collapse a cylindrical shell such that all the initial kinetic energy is dissipated through plastic work and the shell comes to rest at a final 'stopping radius' of r_0'. The initial and transient configurations of the shell are illustrated in Fig. A1.

A.1. Stresses for Cylinder Yield

Using the generalised Hooke's law, and assuming the shell material is incompressible, the state of stress in an elastic cylinder subjected to plane strain ($\epsilon_z = 0$) can be expressed as

$$\begin{aligned} 2\sigma_r - \sigma_\theta - \sigma_z &= 6G\epsilon_r \\ 2\sigma_\theta - \sigma_z - \sigma_r &= -6G\epsilon_r \\ 2\sigma_z - \sigma_r - \sigma_\theta &= 0, \end{aligned} \tag{A1}$$

where σ_r, σ_θ, σ_z are the total stresses acting in the radial, circumferential, and longitudinal directions, respectively, G is the shear modulus, and ϵ_r is the radial strain. To detect the onset of plastic flow we can introduce the von Mises yield condition,

$$(\sigma_1 - \sigma_2)^2 + (\sigma_2 - \sigma_3)^2 + (\sigma_3 - \sigma_1)^2 = 2Y_0^2. \tag{A2}$$

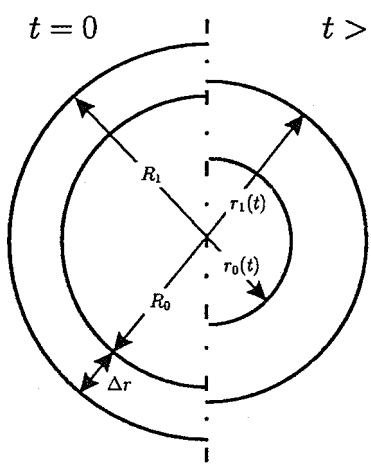

FIG. A1. Initial and transient configuration of cylindrical shell collapse. Here, R_1 and R_0 are the initial outside and inside radii, and $r_1(t)$ and $r_0(t)$ are the outside and inside radii during the collapse.

Since at any point in the cylinder the radial, circumferential, and longitudinal directions are also principal directions, this can be recast as

$$(\sigma_r - \sigma_\theta)^2 + (\sigma_\theta - \sigma_z)^2 + (\sigma_z - \sigma_r)^2 = 2Y_0^2, \tag{A3}$$

where Y_0 is the yield stress in simple tension. It follows from the last expression in (A1) that

$$\sigma_z = \frac{\sigma_r + \sigma_\theta}{2}, \tag{A4}$$

which upon substitution into the yield condition, (A3), yields (see Nadai [25])

$$\sigma_\theta - \sigma_r = \frac{2}{\sqrt{3}} Y_0. \tag{A5}$$

Defining the hydrostatic pressure as the mean of the three stresses, we have

$$p = -\frac{1}{3}(\sigma_r + \sigma_\theta + \sigma_z), \tag{A6}$$

or utilising (A4),

$$p = -\frac{1}{2}(\sigma_r + \sigma_\theta). \tag{A7}$$

Combining this pressure definition and the yield condition yields

$$\sigma_r = p - \frac{1}{\sqrt{3}} Y_0 \quad \text{and} \quad \sigma_\theta = p + \frac{1}{\sqrt{3}} Y_0, \tag{A8}$$

which are the stresses required in the radial and circumferential directions to produce yielding of the cylinder.

A.2. Plastic Work Done During Collapse

For cylindrical symmetry the Lagrangian governing equations may be reduced to one-dimensional equations with a geometric source term,

$$\frac{d\rho}{dt} = -\rho\left(\frac{\partial u}{\partial r} + \frac{u}{r}\right) \text{(conservation of mass)} \tag{A9}$$

$$\rho\frac{du}{dt} = \frac{\partial \sigma_r}{\partial r} - \frac{\sigma_\theta - \sigma_r}{r} \text{(conservation of momentum)} \tag{A10}$$

$$\rho\frac{dE}{dt} = \frac{\partial u}{\partial r}\sigma_r + \frac{u}{r}\sigma_\theta \text{(conservation of energy).} \tag{A11}$$

The assumption of incompressibility reduces the continuity equation still further:

$$\frac{\partial u}{\partial r} = -\frac{u}{r}. \tag{A12}$$

Substituting the stresses at yield defined by (A8), the equation for the conservation of energy becomes, for plastic flow,

$$\rho \frac{dE}{dt} = p\left(\frac{\partial u}{\partial r} + \frac{u}{r}\right) - \frac{Y_0}{\sqrt{3}}\left(\frac{\partial u}{\partial r} - \frac{u}{r}\right), \tag{A13}$$

and with the further simplification of incompressibility,

$$\rho \frac{dE}{dt} = -\frac{2Y_0 u}{\sqrt{3}r}. \tag{A14}$$

For a cylinder of inside and outside radii $r_0(t)$ and $r_1(t)$, the rate of change of total internal energy per unit length E_{tot} is given by

$$\frac{dE_{tot}}{dt} = \int_{r_0(t)}^{r_1(t)} 2\pi r \rho \frac{dE}{dt}\, dr. \tag{A15}$$

By assuming the collapse is incompressible, $\epsilon_r + \epsilon_\theta + \epsilon_z = 0$, and for plane strain, $\epsilon_r + \epsilon_\theta = 0$; therefore,

$$\frac{du}{dr} + \frac{u}{r} = 0 \tag{A16}$$

since

$$\epsilon_r = \frac{du}{dr} \quad \text{and} \quad \epsilon_\theta = \frac{u}{r}. \tag{A17}$$

Therefore, a velocity distribution through the shell which satisfies incompressibility can be obtained by integrating (A16),

$$u = \frac{C}{r}, \tag{A18}$$

where C is a constant of integration. Combining (A14), (A15) and (A18) yields

$$\frac{dE_{tot}}{dt} = -\frac{4}{\sqrt{3}}\pi Y_0 C(t) \ln \frac{r_1(t)}{r_0(t)}. \tag{A19}$$

However, since

$$\frac{dE_{tot}}{dr_0(t)} = \frac{r_0(t)}{C(t)}\frac{dE_{tot}}{dt} \quad \text{and} \quad \frac{dE_{tot}}{dx} = R_0 \frac{dE_{tot}}{dr_0(t)}, \tag{A20}$$

we have

$$\frac{dE_{tot}}{dx} = -\frac{4}{\sqrt{3}}\pi Y_0 x R_0^2 \ln \frac{r_1(t)}{r_0(t)}, \tag{A21}$$

where we define $x = r_0(t)/R_0$. Using the relationship $R_1^2 - R_0^2 = r_1^2(t) - r_0^2(t)$, where R_0 and R_1 are the initial inside and outside radii, we can eliminate $r_1(t)$ and $r_0(t)$ from (A21) to yield

$$\frac{dE_{tot}}{dx} = -\frac{2}{\sqrt{3}}\pi Y_0 x R_0^2 \ln\left(1 + \frac{2\alpha + \alpha^2}{x^2}\right), \tag{A22}$$

where $\alpha = (R_1 - R_0)/R_0$. Integrating,

$$\Delta E_{tot} = \frac{2}{\sqrt{3}} \pi Y_0 R_0^2 F(\alpha, \lambda), \tag{A23}$$

which is equivalent to the plastic work done during the collapse where $\lambda = r_0'/R_0$ and the function $F(\alpha, \lambda)$ is given,

$$F(\alpha, \lambda) = \int_{\lambda}^{1} x \ln\left(1 + \frac{2\alpha + \alpha^2}{x^2}\right) dx. \tag{A24}$$

Note that similar expressions can be obtained as a function of the final outside stopping radius r_1',

$$\Delta E_{tot} = \frac{2}{\sqrt{3}} \pi Y_0 R_1^2 F(z, \xi). \tag{A25}$$

where,

$$F(z, \xi) = \int_{\xi}^{1} z \ln\left(\frac{z^2 R_1^2}{R_0^2 - R_1^2 + z^2 R_1^2}\right) dz, \quad \xi = r_1'/R_1, \quad z = r_1(t)/R_1 \tag{A26}$$

A cylindrical shell with an initial outside radius R_1 and inside radius R_0 has an initial kinetic energy per unit length given by,

$$\mathrm{KE} = \frac{1}{2} \int_{R_0}^{R_1} 2\pi r \rho u^2 \, dr \tag{A27}$$

Using $u = C/r$ the initial kinetic energy per unit length can be written,

$$\mathrm{KE} = \pi \rho C^2 \ln \frac{R_1}{R_0} \tag{A28}$$

Since initially $C = u_0 R_0$, where u_0 is the initial velocity at the shell inner face, the initial kinetic energy per unit length is finally,

$$\mathrm{KE} = \pi \rho u_0^2 R_0^2 \ln \frac{R_1}{R_0} \tag{A29}$$

Equating the plastic work done during the collapse to the initial kinetic energy, and rearranging for u_0 yields,

$$u_0 = \sqrt{\frac{2 Y_0 F(\alpha, \lambda)}{\sqrt{3} \rho \ln(R_1/R_0)}} \tag{A30}$$

where the function $F(\alpha, \lambda)$ requires numerical integration for the configuration of interest.

ACKNOWLEDGMENTS

This research was funded by the Atomic Weapons Establishment, Aldermaston, UK. The authors are grateful to Andrew Barlow (AWE) for much valuable advice and to *Century Dynamics Ltd.* for permission to use their AUTODYN-2D software for comparison with the techniques developed in this paper.

REFERENCES

1. S. Armfield and R. Street, The fractional-step method for the Navier–Stokes equations on staggered grids: the accuracy of the three variations, *J. Comput. Phys.* **153**, 660 (1999).
2. C. J. Ball, A Free-Lagrange method for unsteady compressible flow: simulation of a confined cylindrical blast wave, *Shock Waves* **5**, 311 (1996).
3. C. J. Ball, B. P. Howell, T. G. Leighton, and M. J. Schofield, Shock-induced collapse of a cylindrical air cavity in water: a Free-Lagrange simulation, *Shock Waves* **10**, 265 (2000).
4. P. Batten, D. M. Ingram, R. Saunders, and D. M. Causon, A time-splitting approach to solving the Navier–Stokes equations, *Compute. Fluids* **24**(4), 421 (1996).
5. N. K. Birnbaum, M. S. Cowler, M. Itoh, M. Katayama, and H. Obata, AUTODYN-An interactive non-linear dynamics analysis program for the microcomputers through to supercomputers, in *Transactions of the 9th International Conference on Structural Mechanics in Reactor Technology*, (Balkema, Rotterdam/Boston, 1987), Vol. B, pp. 401–406.
6. E. J. Caramana, Timestep relaxation with symmetry preservation on high aspect-ratio angular or tapered grids, *J. Comput. Phys.* **166**, 173 (2001).
7. E. J. Caramana, D. E. Burton, M. J. Shashkov, and P. P. Whalen, The construction of compatible hydrodynamics algorithms utilizing conservation of total energy, *J. Comput. Phys.* **146**, 227 (1998).
8. E. J. Caramana and M. J. Shashkov, Elimination of artificial grid distortion and hourglass-type motions by means of Lagrangian subzonal masses and pressures, *J. Comput. Phys.* **142**, 521 (1998).
9. E. J. Caramana and P. P. Whalen, Numerical preservation of symmetry properties of continuum problems, *J. Comput. Phys.* **141**, 174 (1998).
10. J. P. Cocchi, R. Saurel, and J. C. Loraud, Treatment of interface problems with Godunov-type schemes, *Shock Waves* **5**, 347 (1996).
11. J. K. Dukowicz, A general, non-iterative Riemann solver for Godunov's method, *J. Comput. Phys.* **61**, 119 (1985).
12. M. J. Fritts, W. P. Crowley, and H. Trease, Eds., *The Free-Lagrange Method*, Lecture Notes in Physics (Springer-Verlag, Berlin/Heidelberg/New York/Tokyo, (1985), Vol. 238.
13. P. J. Green and R. Sibson, Computing Dirichlet tessellations in the plane, *Comp. J.* **21**, 168 (1978).
14. W. H. Gust, High impact deformation of metal cylinders at elevated temperatures, *J. Appl. Phys.* **53**(5), 3566 (1982).
15. J. O. Hallquist, *NIKE2D-A Vectorized Implicit, Finite Deformation Finite Element Code for Analyzing the Static and Dynamic Response of 2D Solids with Interactive Rezoning and Graphics*, Lawrence Livermore National Laboratory, Technical Report UCID-19677, Rev. 1 (1986).
16. F. H. Harlow and A. A. Amsden, *Fluid Dynamics*, Los Alamos Scientific Laboratory Technical Report LA-4700 (1971).
17. B. P. Howell, *An Investigation of Lagrangian Riemann Methods Incorporating Material Strength*, Ph.D. thesis (University of Southampton, 2000).
18. B. P. Howell and G. J. Ball, Damping of mesh-induced errors in Free-Lagrange simulations of Richtmyer–Meshkov instability, *Shock Waves* **10**, 253 (2000).
19. B. L. Keyfitz and H. C. Kranzer, A system of non-strictly hyperbolic conservation laws arising in elastic theory, *Arch. Rat. Mech. Anal.* **72**, 220 (1980).
20. X. Lin and J. Ballmann, A Riemann solver and second-order Godunov method for elastic–plastic wave propagation in solids, *Int. J. Impact Eng.* **13**(3), 463 (1993).
21. T. P. Liu, The Riemann problem for general systems of conservation laws, *J. Diff. Eq.* **18**, 218 (1975).
22. G. H. Miller and E. G. Puckett, A high-order Godunov method for multiple condensed phases, *J. Comput. Phys.* **128**, 134 (1996).
23. G. H. Miller and P. Colella, A high-order Eulerian Godunov method for elastic–plastic flow in solids, *J. Comput. Phys.* **167**, 131 (2001).
24. J. J. Monaghan, On the problem of penetration in particle methods, *J. Comput. Phys.* **82**, 1 (1989).
25. A. Nadai, *Theory of Flow and Fracture of Solids* (McGraw–Hill, New York, 1950).

26. B. J. Plohr, Shockless acceleration of thin plates modeled by a random choice method, *AIAA J.* **26**(4), 470 (1988).
27. D. Rhynsburger, Analytic delineation of Thiessen polygons, *Geog. Anal.* **5**, 133 (1973).
28. T. D. Riney, Numerical evaluation of hypervelocity impact phenomena, in *High Velocity Impact Phenomena*, edited by R. Kinslow (Academic Press, New York/London, 1970), pp. 157–212.
29. P. J. Roache, Perspective: A method for uniform reporting of grid refinement studies, *J. Fluids Eng.* **116**, 405 (1994).
30. M. Shearer, The Riemann problem for a class of conservation laws of mixed type, *J. Diff. Eq.* **46**, 426 (1982).
31. D. J. Steinberg, S. G. Cochran, and M. W. Guinan, A constitutive model for metals applicable at high-strain rate, *J. Appl. Phys.* **51**(3), 1498 (1980).
32. H. F. Swift, Hypervelocity impact mechanics, in *Impact Dynamics*, edited by J. A. Zukas, T. Nicholas, H. F. Swift, L. B. Greszczuk, and D. R. Curran (Wiley, New York, 1982), pp. 215–239.
33. H. S. Tang and F. Sotiropoulos, A second-order Godunov method for wave problems in coupled solid–water–gas systems, *J. Comput. Phys.* **151**, 790 (1999).
34. A. Tang and T. Ting, Wave curves for the Riemann problem of plane waves in elastic solids, *Int. J. Eng. Sci.* **25**, 1343 (1987).
35. E. F. Toro and R. E. Brown, The WAF method and splitting procedures for viscous shocked flows, in *Proceedings of the 18th International Symposium on Shock Waves, Sendai, Japan,* (Springer-Verlag, Berlin/ New York, 1992), pp. 1119–1126.
36. E. F. Toro, *Riemann Solvers and Numerical Methods for Fluid Dynamics: A Practical Introduction* (Springer-Verlag, Berlin/New York, 1997).
37. J. A. Trangenstein and P. Colella, A higher-order Godunov method for modelling finite deformation in elastic–plastic solids, *Commun. Pure Appl. Math.* **10**, 41 (1991).
38. J. A. Trangenstein and R. B. Pember, The Riemann problem for longitudinal motion in an elastic–plastic bar, *SIAM J. Sci. Stat. Comput.* **12**, 180 (1991).
39. M. B. Tyndall, Numerical modelling of shocks in solids with elastic–plastic conditions, *Shock Waves* **3**, 55 (1993).
40. M. B. Tyndall, *Numerical Modelling of Shock Waves in Solid Materials*, Ph.D. thesis (Monash University, 1991).
41. D. Verney, Évaluation de la limite élastique du cuivre et de l'uranium par des expériences d'implosion 'lente', in *Behavior of Dense Media Under High Dynamic Pressures, Symposium H.D.P., Paris, September 1968* (Gordon & Breach, New York, 1968).
42. C. T. Wang, *Applied Elasticity* (McGraw–Hill, New York, 1953).
43. L. Weixen, Simplified equation of state $P = P(\rho, E)$ and $P = P(\rho, T)$ for condensed matter, in *Shock Waves in Condensed Matter*, edited by Y. M. Gupta (Plenum Press, New York, 1986), pp. 167–173.
44. B. Wendroff, The Riemann problem for materials with nonconvex equations of state I: Isentropic flow, *J. Math. Anal. Appl.* **38**, 454 (1972).
45. M. L. Wilkins, Calculation of elastic–plastic flow, *Meth. Comput. Phys.* **3**, 211 (1964).
46. N. N. Yanenko, *The Method of Fractional Steps* (Springer-Verlag, Berlin/New York, 1971).
47. J. A. Zukas, Survey of computer codes for impact simulation, in *High Velocity Impact Dynamics*, edited by J. A. Zukas (Wiley, New York, 1990), pp. 593–708.
48. Prepared by Group GMX-6, *Selected Hugoniots* (Los Alamos Scientific Laboratory, University of New Mexico, Los Alamos, LA-4167-MS, 1969).